Localized necking predictions based on rate-independent self-consistent polycrystal plasticity: Bifurcation analysis versus imperfection approach

Holanyo Akpama, Mohamed Ben Bettaieb, Farid Abed-Meraim

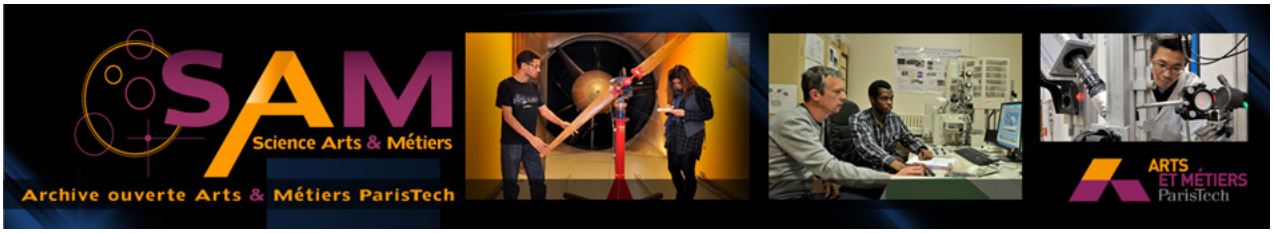

Localized necking predictions based on rate-independent self-consistent polycrystal plasticity: Bifurcation analysis versus imperfection approach

H.K. Akpama [a, b], M. Ben Bettaieb [a, b, *], F. Abed-Meraim [a, b]

[a] *Laboratoire d'Étude des Microstructures et de Mécanique des Matériaux (LEM3), UMR 7239, CNRS/Arts et Métiers ParisTech, 4 rue Augustin Fresnel, 57078, Metz Cedex 3, France*
[b] *DAMAS, Laboratory of Excellence on Design of Alloy Metals for low-mAss Structures, Université de Lorraine, France*

A B S T R A C T

The present study focuses on the development of a relevant numerical tool for predicting the onset of localized necking in polycrystalline aggregates. The latter are assumed to be representative of thin metal sheets. In this tool, a micromechanical model, based on the rate-independent self-consistent multi-scale scheme, is developed to accurately describe the mechanical behavior of polycrystalline aggregates from that of their single crystal constituents. In the current paper, the constitutive framework at the single crystal scale follows a finite strain formulation of the rate-independent theory of crystal elasto-plasticity. To predict the occurrence of localized necking in polycrystalline aggregates, this micromechanical modeling is combined with two main strain localization approaches: the bifurcation analysis and the initial imperfection method. The formulation of both strain localization indicators takes into consideration the plane stress conditions to which thin metal sheets are subjected during deformation. From a numerical point of view, strain localization analysis with this crystal plasticity approach can be viewed as a strongly non-linear problem. Hence, several numerical algorithms and techniques are developed and implemented in the aim of efficiently solving this non-linear problem. Various simulation results obtained by the application of the developed numerical tool are presented and extensively discussed. It is demonstrated from these results that the predictions obtained with the Marciniak–Kuczynski procedure tend towards those yielded by the bifurcation theory, when the initial imperfection ratio tends towards zero. Furthermore, the above result is shown to be valid for both scale-transition schemes, namely the full-constraint Taylor model and self-consistent scheme.

1. Introduction

In the field of material ductility, in general, and more particularly in relation to sheet metal formability, localized necking, which may sometimes lead to fracture, has for a long time attracted interest of metallurgists and scientists. In spite of the important advances achieved in understanding these plastic instability phenomena, the modeling of localized necking

remains an active research topic. In this field, one can quote the pioneering work of Keeler and Backofen (1963), who originally developed the now classical concept of Forming Limit Diagram (FLD). Because of the practical difficulties related to the experimental quantification of the FLDs (Li et al., 2013), as well as their relatively high cost, particular attention has been focused on setting up reliable analytical and/or numerical models for predicting these FLDs (Zadpoor et al., 2009; Stoughton and Yoon, 2011; Chung et al., 2014; Manopulo et al., 2015). These alternative approaches require the use of a constitutive framework, to follow the evolution of the variables defining the mechanical state of the sheet metal, in conjunction with a localization criterion in order to numerically determine the inception of strain localization. For a long time, models based on a phenomenological description of the mechanical behavior have been employed to predict the FLDs of thin metal sheets. In this regard, one can quote Hill (1952), who used a phenomenological isotropic rigid-plastic model, along with an instability criterion nowadays known as the Hill'52 approach, to predict the formability limits in the negative strain-path range. Later, Marciniak and Kuczynski (1967) developed an approach based on the existence of an initial imperfection and coupled this localization criterion with an isotropic rigid-plastic constitutive framework in order to determine the right-hand side of the FLD. In most of the works devoted to the numerical prediction of FLDs, it is observed that both the shape and the location of these diagrams are extremely sensitive to the mechanical and physical properties. Accordingly, a wide range of phenomenological behavior models have been coupled with various localization criteria to assess the influence of some constitutive features, such as for instance strain-rate sensitivity (Khan and Baig, 2011), plastic anisotropy (Zhang and Wang, 2012), and damage-induced softening (Haddag et al., 2009; Abed-Meraim et al., 2014; Mansouri et al., 2014). Despite their good predictive capabilities, the phenomenological models, which are the most widely used for the prediction of FLDs, are not able to account for some essential physical and mechanical features, such as initial and induced textures and other microstructure-related parameters (grain morphology, crystallographic structure …). These limitations represent the main motivations behind the more recent use of micromechanical modeling for the FLD prediction. The advantage of such physically-based modeling, compared to phenomenological approaches, is its ability to link, in a natural way, the material microstructure to some important in-use properties (strength, formability …). Indeed, in micromechanical modeling, the constitutive relations are expressed at the single crystal level, and account for mechanisms relevant at this scale in the description of the hardening, such as the slip of crystallographic planes, lattice rotation, dislocation motion … The constitutive relations of the polycrystalline aggregate are derived from those of its components (i.e., single crystals) on the basis of some scale-transition schemes. Therefore, prediction of FLDs based on micromechanical modeling requires three main ingredients: constitutive modeling at the scale of the single crystal, a multi-scale scheme to determine the mechanical behavior of the polycrystalline material, and a localization approach to predict the initiation of strain localization.

- **Modeling at the single crystal scale:** In order to predict FLDs via micromechanical approaches, various constitutive frameworks have been adopted to model the mechanical behavior at the single crystal scale. These constitutive models, formulated within a finite strain framework, can be categorized as follows: rate-dependent and rate-independent frameworks. Within the family of rate-dependent approaches, one can quote for instance the works of Neil and Agnew (2009), Signorelli et al. (2009), Lévesque et al. (2010), Schwindt et al. (2015). As to the family of rate-independent approaches, fewer contributions have been done, among which Knockaert et al. (2002), Franz et al. (2009a, 2009b, 2013), Yoshida and Kuroda (2012). The crystallographic structures considered in the above-mentioned investigations are of cubic type (namely FCC and BCC structures). In the present investigation, a rate-independent framework is adopted to model the mechanical behavior of FCC single crystals. Nevertheless, this formulation can be easily generalized to other crystallographic structures, such as HCP or BCC. The plastic deformation, which is taken to be solely due to the shear over the slip systems, is modeled by using the Schmid rule. The evolution of the critical shear stresses is expressed through a power-type hardening law similar to that used in Yoshida and Kuroda (2012). The constitutive equations associated with the single crystal modeling are strongly non-linear. Consequently, their solving involves a huge amount of CPU time as well as of memory space. This significantly increases the CPU time required for FLD predictions, especially for realistic and representative polycrystalline aggregates, which are made of a large number of grains (typically more than 1000 grains). To deal with these large computations, an efficient and robust numerical scheme is implemented to integrate the single crystal constitutive equations (Ben Bettaieb et al., 2012; Akpama et al., 2016). This algorithm is implicit and belongs to the family of ultimate algorithms, which has been shown to be more efficient than return-mapping algorithms (Akpama et al., 2016). To enhance the efficiency of the developed algorithm, a semi-smooth formulation of the consistency condition, based on the Fischer–Burmeister complementarity functions, is used. This semi-smooth formulation allows merging two tasks: the determination of the set of active slip systems, and the calculation of the corresponding slip rates. This strategy leads to a significant reduction in the CPU time required for the integration of the constitutive equations at the single crystal scale.
- **Scale-transition scheme:** In the literature, different scale-transition schemes have been elaborated to derive the overall mechanical behavior of polycrystals from the mechanical behavior of single crystals. Such aggregates are assumed to be representative of the studied sheet metal. Among the well-known scale-transition schemes, the full-constraint Taylor approach (briefly called the Taylor model in what follows) is known to be the earliest and one of the most commonly used micromechanical models to predict the mechanical behavior of polycrystalline aggregates. The wide use of this model is due to its simplicity and its easy numerical implementation, as compared to other multiscale schemes, such as the self-consistent approach or the Crystal Plasticity Finite Element Method (CPFEM). This Taylor model is based on the

assumption of the uniformity of the local (microscopic) deformation field over the polycrystalline aggregate. Indeed, in this model, it is assumed that all the single crystals composing the polycrystalline aggregate undergo the same strain field as the macroscopic one. However, it has been demonstrated that, theoretically, textures predicted by the Taylor model are much sharper, i.e. more pronounced, than those observed experimentally (Dillamore and Katoh, 1974; Harren et al., 1989). This was attributed to the local nonuniform deformations, which occur in real polycrystals, that the Taylor model cannot address. This implies that the condition of uniform deformation imposed within the Taylor model is not physically realistic. Furthermore, the equilibrium condition is not fully satisfied when the Taylor model is used. Other theories, such as those called "self-consistent theories", seem to be more appropriate than the Taylor scheme to model polycrystal plasticity of strongly anisotropic materials. Indeed, self-consistent approaches are able to address in a much better way the issues related to the uniformity of the deformation fields and the violation of the equilibrium condition, since they account for grain interactions. Another main difference between the Taylor and self-consistent models is related to the modeling of the grain morphology. Indeed, within the Taylor model, the description of the grain morphology is relatively poor and inaccurate, since this morphology is basically defined by the volume fraction of the corresponding grain. However, within the self-consistent model, the morphology of each grain is defined by its volume fraction and its shape. The modeling as well as the evolution of the grain shape is a very important factor that should be accounted for during large plastic deformations of metals (Ahzi et al., 1990). In summary, the self-consistent model is able to take into account three properties that are not considered in the Taylor model: the local nonuniformity of the deformation field, which is due to the texture evolution, the equilibrium condition, and the grain shape. Therefore, it is expected that the self-consistent scheme is more realistic and more accurate than the Taylor model in the modeling of plastic deformations of polycrystalline metals. The superiority of the self-consistent approach, compared to the Taylor model, has been demonstrated in the literature by comparing its numerical predictions with several experimental results (see, for instance, Wenk et al., 1988; Lebensohn and Tomé, 1994; Signorelli et al., 2009; Jeong et al., 2016). Hence, we believe that the self-consistent model is physically more realistic than the Taylor model. In the current paper, the self-consistent model is used in conjunction with a rate-independent single crystal plasticity formulation. This formulation is more suitable and more realistic than the rate-dependent one for the modeling of cold forming processes, which usually exhibit very low sensitivity to the strain rate. Within the self-consistent approach, each single crystal is assumed to be an ellipsoidal inclusion contained in a fictitious homogeneous medium endowed with the same mechanical features as the polycrystalline aggregate. The current formulation of the self-consistent model is founded on the theoretical developments of Lipinski and Berveiller (1989). From a numerical point of view, the self-consistent scheme may be regarded as a non-linear problem. This non-linear problem is traditionally solved by using the fixed point method, where the main unknown is the macroscopic (overall) tangent modulus. When the rate-dependent formulation is used, all of the slip systems are assumed to be active. Hence, as there is no change in activity of the slip systems during the loading, the components of the macroscopic tangent modulus computed by the self-consistent scheme evolve slowly and without abrupt changes. Therefore, the observed change in these components between the beginning and the end of a typical time increment is very moderate. Consequently, the fixed point method used to solve the governing self-consistent equations, within a rate-dependent formulation, converges always and rapidly. However, when the rate-independent formulation is used (which is the case in the current paper), the set of active slip systems may change from one increment to another and, accordingly, abrupt changes in the components of the macroscopic tangent modulus may occur during the loading. These abrupt changes lead to several numerical difficulties when the fixed point method is applied. Indeed, contrary to the rate-dependent formulation, the convergence of the fixed point method is not always guaranteed when the self-consistent approach is applied within a rate-independent formulation. For these reasons, and to avoid the above-discussed numerical issues, we have developed a new algorithm (alternative to the fixed point method), based on the Newton–Raphson method, to solve the self-consistent equations. This new algorithm is used when the fixed point method fails to converge. As well-known from several other classical numerical problems, and confirmed by the numerical developments carried out in the current paper, the use of the Newton–Raphson algorithm ensures quasi-permanent convergence but requires a CPU time larger than that required when the fixed point method is applied (as a Jacobian matrix should be computed and inverted at each iteration). To our best knowledge, this is the first time the Newton–Raphson algorithm is used to solve the self-consistent equations.

- **Strain localization prediction:** Two main categories of strain localization theories can be coupled with micromechanical models in order to predict FLDs: the imperfection approach and the bifurcation analysis. As mentioned above, the imperfection approach was originally introduced by Marciniak and Kuczynski (1967). For brevity, this procedure will be called hereafter the M–K analysis. The main assumption on which the theoretical framework of this localization criterion is based is the preexistence of an imperfection in the form of local variation in material properties and/or in thickness, which affects the evolution of the mechanical fields and consequently influences the onset of localized necking. Indeed, after the deformation has reached a certain level, it starts concentrating much more in the imperfection zone than in the remaining homogeneous part, thus leading to localized necking. In the literature, the M–K approach has been most often coupled with phenomenological constitutive models (Stoughton and Zhu, 2004; Allwood and Shouler, 2009; Eyckens et al., 2011). However, in recent years, this imperfection theory has also been combined with micromechanical models. For instance, it has been coupled with the Taylor model to predict FLDs for elasto-viscoplastic materials (Lévesque et al., 2010) as well as for elasto-plastic materials (Knockaert et al., 2002; Yoshida and Kuroda, 2012). The coupling of the M–K analysis with the self-consistent multi-scale scheme has been first achieved in Signorelli et al. (2009). In this pioneering work, the mechanical behavior of the single crystals has been described by a viscoplastic rate-dependent model. Signorelli

et al. (2009) have demonstrated that the FLDs obtained by using the self-consistent multiscale scheme agree well with the experimental FLDs. However, they show that the Taylor model severely underestimates the experimentally observed limit strains over the complete range of positive strain paths. Note that the experimental results they have used for the comparison between the two multiscale models were taken from Viatkina et al. (2005). In more recent works, the experimental FLDs of the AA5182-O alloy and the electro-galvanized DQ-type steel have been compared with the predicted ones in Serenelli et al. (2011) and Signorelli et al. (2012), respectively. For both materials (namely the AA5182-O alloy and the electro-galvanized DQ-type steel), the authors have demonstrated that the self-consistent model allows realistic predictions over the entire FLD, while the predictions obtained by the Taylor model only follow the experimentally measured limit curve in the range of negative strain paths. In the range of positive strain paths, however, the Taylor model predicts unrealistically low (resp. high) limit strain values for the AA5182-O alloy (resp. the electro-galvanized DQ-type steel). The consistency of the predictions based on the self-consistent model suggests that this model reveals to be a more suitable tool for describing the role of crystallographic textures in sheet metal forming processes. These comparisons with experiments confirm the idea according to which the self-consistent model is physically more realistic than the Taylor model. In the present work, however, it is within a rate-independent constitutive framework that the self-consistent multi-scale scheme is applied to derive the overall properties of elasto-plastic polycrystalline aggregates, and then to determine the onset of strain localization through its coupling with the M−K analysis. To the authors' best knowledge, this is the first time the M−K analysis is combined with a rate-independent self-consistent polycrystal model for the FLD prediction. The equations governing the M−K analysis mainly consist of two relations: the compatibility condition and the equilibrium equation. The combination of these two equations results in a highly non-linear system. These resulting equations are efficiently solved by the fixed point method.

The second localization criterion adopted in this work is based on bifurcation theory (Rice, 1976). With this approach, the localization phenomenon is viewed as a consequence of instability in the constitutive description of uniform deformation. In other words, the occurrence of strain localization is a result of jump in the macroscopic velocity gradient of the deformed solid. It is noteworthy that, besides its sound theoretical foundations, the bifurcation approach does not need the calibration of any additional parameter, such as the geometric imperfection factor required when the M−K analysis is used. However, without the presence of some destabilizing effects, localized necking is detected at unrealistically high strain levels in the range of positive in-plane biaxial stretching (Ben Bettaieb and Abed-Meraim, 2015). A similar trend is observed when the mechanical behavior exhibits strain-rate sensitivity. Indeed, for elasto-viscoplastic materials, the predicted limit strains are very high because they are entirely controlled by elasticity. By contrast, in the rate-independent framework, the application of the bifurcation approach in conjunction with a micromechanical model provides realistic forming limits. The main reason for these observations is that typical destabilizing effects are an inherent result in the application of crystal plasticity, through the formation of vertices at the current points of the Schmid yield locus. In this field, Franz et al. (2009a, 2009b, 2013) have investigated the forming limits of various BCC materials by using the self-consistent approach along with crystal elasto-plasticity coupled with bifurcation analysis. It is noteworthy that their predictions were carried out in the framework of a general three-dimensional formulation, thus allowing out-of-plane localization modes to be considered. Alternatively, Yoshida and Kuroda (2012) used the bifurcation criterion in conjunction with the Taylor model to predict FLDs for FCC materials. In their work, a two-dimensional formulation has been adopted (i.e., the localization band is assumed to lie in the plane of the sheet). The same type of approach is followed in the current contribution, except that the self-consistent multi-scale model is used instead of the Taylor model. The motivation behind this choice of a two-dimensional formulation for the bifurcation criterion is to allow comparisons between the predicted FLDs and those yielded by the initial imperfection approach (which usually follows a two-dimensional formulation). Besides the development of very powerful and efficient numerical tools for the prediction of ductility limits (which is, from the authors' perspective, an important originality in the current paper), we have also demonstrated another original result: when the initial imperfection ratio involved in the initial imperfection analysis tends towards zero, the associated FLDs tend towards the bifurcation-based FLD. It is noteworthy that this important result, which has already been demonstrated for phenomenological constitutive models (see, e.g., Ben Bettaieb and Abed-Meraim, 2015), is shown here to be valid for both scale-transition schemes, namely the Taylor model and the self-consistent scheme. Of course, such a comparison between the predictions given by the bifurcation theory and those yielded by the M−K analysis is not possible when the mechanical behavior is taken to be rate-dependent.

The reminding parts of the paper are structured as follows:

- ✓ The second Section is devoted to the presentation of the single crystal constitutive equations and the corresponding algorithmic aspects.
- ✓ The third Section provides the main lines of the self-consistent transition scheme used to obtain the overall polycrystalline behavior as well as the corresponding numerical implementation.
- ✓ The theoretical frameworks for the two strain localization approaches (the bifurcation theory and the initial imperfection analysis) and the related numerical implementations are presented in the fourth Section.
- ✓ In the fifth Section, various numerical results are provided, which illustrate the key features pertaining to the bifurcation approach and the M−K analysis.

2. Single crystal constitutive modeling

2.1. Theoretical framework

The following multiplicative decomposition of the total deformation gradient $\mathbf{f}$ into its elastic part $\mathbf{f}^{e}$ and its plastic part $\mathbf{f}^{p}$ is adopted (see Fig. 1):

$$\mathbf{f} = \mathbf{f}^{e}\cdot\mathbf{f}^{p}. \tag{1}$$

Furthermore, the polar decomposition of $\mathbf{f}^{e}$ allows interpreting the latter as a pure rotation tensor $\mathbf{r}$ followed by a stretching tensor $\mathbf{v}^{e}$.

$$\mathbf{f}^{e} = \mathbf{v}^{e}\cdot\mathbf{r}. \tag{2}$$

Tensor $\mathbf{r}$ maps the relative orientation of the intermediate configuration coordinate system with respect to the frame that is tied to the current configuration (also called deformed configuration).

Using Eqs. (1) and (2), the Eulerian velocity gradient $\mathbf{g}$ takes the following form:

$$\mathbf{g} = \dot{\mathbf{f}}\cdot\mathbf{f}^{-1} = \dot{\mathbf{f}}^{e}\cdot\mathbf{f}^{e-1} + \mathbf{f}^{e}\cdot\dot{\mathbf{f}}^{p}\cdot\mathbf{f}^{p-1}\cdot\mathbf{f}^{e-1} = \dot{\mathbf{v}}^{e}\cdot\mathbf{v}^{e-1} + \mathbf{v}^{e}\cdot\dot{\mathbf{r}}\cdot\mathbf{r}^{T}\cdot\mathbf{v}^{e-1} + \mathbf{v}^{e}\cdot\mathbf{r}\cdot\dot{\mathbf{f}}^{p}\cdot\mathbf{f}^{p-1}\cdot\mathbf{r}^{T}\cdot\mathbf{v}^{e-1}, \tag{3}$$

where $\bullet^{-1}$ (resp. $\dot{\bullet}$) denotes the inverse (resp. the time derivative) of tensor $\bullet$.

It is widely admitted, due to the very low magnitude of the elastic strain in most metallic materials, that the corresponding elastic stretching tensor $\mathbf{v}^{e}$ is almost equal to the second-order identity tensor $\mathbf{I}_2$.

$$\mathbf{v}^{e} \approx \mathbf{I}_2. \tag{4}$$

Combining Eqs. (3) and (4), one obtains

$$\mathbf{g} = \dot{\mathbf{v}}^{e} + \dot{\mathbf{r}}\cdot\mathbf{r}^{T} + \mathbf{r}\cdot\dot{\mathbf{f}}^{p}\cdot\mathbf{f}^{p-1}\cdot\mathbf{r}^{T}. \tag{5}$$

The skew-symmetric and symmetric parts of $\mathbf{g}$, designated as $\mathbf{w}$ and $\mathbf{d}$, respectively, are expressed as follows:

$$\mathbf{w} = \frac{1}{2}\left(\mathbf{g}-\mathbf{g}^{T}\right) = \mathbf{w}^{e}+\mathbf{w}^{p} \quad ; \quad \mathbf{d} = \frac{1}{2}\left(\mathbf{g}+\mathbf{g}^{T}\right) = \mathbf{d}^{e}+\mathbf{d}^{p}, \tag{6}$$

where $\bullet^{T}$ denotes the transpose of tensor $\bullet$. The elastic and plastic parts, $\mathbf{w}^{e}$ and $\mathbf{w}^{p}$, of the rotation rate tensor $\mathbf{w}$, as well as the elastic and plastic parts, $\mathbf{d}^{e}$ and $\mathbf{d}^{p}$, of the strain rate tensor $\mathbf{d}$ are given by

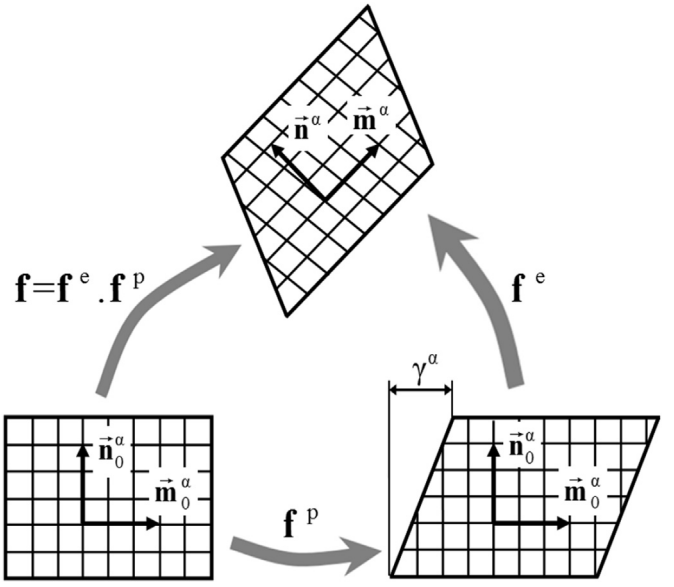

Fig. 1. Graphical illustration of the multiplicative decomposition of the total deformation gradient.

$$\begin{aligned}
&\mathbf{w}^{e} = \mathbf{w} - \mathbf{w}^{p} = \dot{\mathbf{r}}\cdot\mathbf{r}^{T} \quad ; \quad \mathbf{w}^{p} = \frac{1}{2}\mathbf{r}\cdot\left(\dot{\mathbf{f}}^{p}\cdot\mathbf{f}^{p-1} - \left(\dot{\mathbf{f}}^{p}\cdot\mathbf{f}^{p-1}\right)^{T}\right)\cdot\mathbf{r}^{T} \\
&\mathbf{d}^{e} = \dot{\mathbf{v}}^{e} \quad ; \quad \mathbf{d}^{p} = \frac{1}{2}\mathbf{r}\cdot\left(\dot{\mathbf{f}}^{p}\cdot\mathbf{f}^{p-1} + \left(\dot{\mathbf{f}}^{p}\cdot\mathbf{f}^{p-1}\right)^{T}\right)\cdot\mathbf{r}^{T}.
\end{aligned} \tag{7}$$

Each crystallographic slip system α is entirely defined in the current configuration by two vectors $\overrightarrow{\mathbf{m}}^{\alpha}$ and $\overrightarrow{\mathbf{n}}^{\alpha}$ denoting, respectively, the slip direction and the normal to the slip plane. The skew-symmetric and symmetric parts of the tensor product $\overrightarrow{\mathbf{m}}^{\alpha}\otimes\overrightarrow{\mathbf{n}}^{\alpha}$ are denoted by $\mathbf{S}^{\alpha}$ and $\mathbf{R}^{\alpha}$, respectively. In the intermediate configuration, the counterparts of $\overrightarrow{\mathbf{m}}^{\alpha}$ and $\overrightarrow{\mathbf{n}}^{\alpha}$, which are denoted respectively by $\overrightarrow{\mathbf{m}}_{0}^{\alpha}$ and $\overrightarrow{\mathbf{n}}_{0}^{\alpha}$, remain fixed during the deformation. Similarly, the counterparts of tensors $\mathbf{R}^{\alpha}$ and $\mathbf{S}^{\alpha}$, expressed in the intermediate configuration, are denoted by $\mathbf{R}_{0}^{\alpha}$ and $\mathbf{S}_{0}^{\alpha}$, respectively. The relations between $\overrightarrow{\mathbf{m}}^{\alpha}$ and $\overrightarrow{\mathbf{m}}_{0}^{\alpha}$, respectively, $\overrightarrow{\mathbf{n}}^{\alpha}$ and $\overrightarrow{\mathbf{n}}_{0}^{\alpha}$ are given by the following expressions (see illustration in Fig. 1):

$$\overrightarrow{\mathbf{m}}^{\alpha} = \mathbf{f}^{e}\cdot\overrightarrow{\mathbf{m}}_{0}^{\alpha} \quad ; \quad \overrightarrow{\mathbf{n}}^{\alpha} = \overrightarrow{\mathbf{n}}_{0}^{\alpha}\cdot\mathbf{f}^{e-1}. \tag{8}$$

By considering Eq. (4), relations (8) can be transformed into

$$\overrightarrow{\mathbf{m}}^{\alpha} = \mathbf{r}\cdot\overrightarrow{\mathbf{m}}_{0}^{\alpha} \quad ; \quad \overrightarrow{\mathbf{n}}^{\alpha} = \overrightarrow{\mathbf{n}}_{0}^{\alpha}\cdot\mathbf{r}^{T}. \tag{9}$$

The numbering of vectors $\overrightarrow{\mathbf{m}}_{0}^{\alpha}$ and $\overrightarrow{\mathbf{n}}_{0}^{\alpha}$ for FCC single crystals can be found in Ben Bettaieb et al. (2012).

The plastic deformation is assumed here to be solely the result of the slip on the crystallographic slip systems. Tensors $\mathbf{d}^{p}$ and $\mathbf{w}^{p}$ can be expressed as

$$\mathbf{d}^{p} = \dot{\gamma}^{\alpha}\,\mathrm{sgn}(\tau^{\alpha})\mathbf{R}^{\alpha} \quad ; \quad \mathbf{w}^{p} = \dot{\gamma}^{\alpha}\,\mathrm{sgn}(\tau^{\alpha})\,\mathbf{S}^{\alpha} \quad ; \quad \alpha = 1,\ldots,N_{s}, \tag{10}$$

where:

- $\dot{\gamma}^{\alpha}$ denotes the absolute value of the slip rate corresponding to the slip system α.
- N_{s} stands for the total number of crystallographic slip systems (equal to 12 for FCC single crystals).

It must be noted that Einstein's summation convention over repeated indices is used in Eq. (10) and in the remainder of the paper. Also, the range of dummy (resp. free) index is given after (resp. before) the corresponding equation.

To satisfy the objectivity principle, the co-rotational derivative $\boldsymbol{\sigma}^{J}$ of the Cauchy stress tensor $\boldsymbol{\sigma}$ is introduced. Tensor $\boldsymbol{\sigma}^{J}$ is linked to $\dot{\boldsymbol{\sigma}}$ and $\mathbf{d}^{e}$ by

$$\boldsymbol{\sigma}^{J} = \dot{\boldsymbol{\sigma}} + \boldsymbol{\sigma}.\mathbf{w}^{e} - \mathbf{w}^{e}.\boldsymbol{\sigma} = \mathbf{l}^{e}\colon\mathbf{d}^{e}, \tag{11}$$

where $\mathbf{l}^{e}$ is the elasticity tensor. For the model developed in the present paper, elasticity is assumed to be linear and isotropic.

The resolved shear stress τ^{α} is expressed in terms of $\boldsymbol{\sigma}$ by

$$\forall\ \alpha = 1,\ldots,N_{s}\colon \quad \tau^{\alpha} = \left(\boldsymbol{\sigma}\,.\,\overrightarrow{\mathbf{n}}^{\alpha}\right)\,.\,\overrightarrow{\mathbf{m}}^{\alpha} = \mathbf{R}^{\alpha}:\boldsymbol{\sigma}. \tag{12}$$

The following expression for $\dot{\tau}^{\alpha}$ is obtained by combining Eqs. (10) (11), and (12):

$$\begin{aligned}
\forall\ \alpha = 1,\ldots,N_{s}: \quad \dot{\tau}^{\alpha} &= \mathbf{R}^{\alpha}:\boldsymbol{\sigma}^{J} = \mathbf{R}^{\alpha}:\mathbf{l}^{e}:\left(\mathbf{d} - \dot{\gamma}^{\beta}\,\mathrm{sgn}\left(\tau^{\beta}\right)\mathbf{R}^{\beta}\right) \\
&= \mathbf{R}^{\alpha}\colon\mathbf{l}^{e}\colon\mathbf{d} - \dot{\gamma}^{\beta}\,\mathrm{sgn}\left(\tau^{\beta}\right)\mathbf{R}^{\alpha}:\mathbf{l}^{e}\colon\mathbf{R}^{\beta} \quad ; \quad \beta = 1,\ldots,N_{s},
\end{aligned} \tag{13}$$

where symbol ':' designates the double contraction product.

The plastic flow is governed by the Schmid law. This law expresses that, for a crystallographic system α, slip may occur only if the resolved shear stress τ^{α} becomes equal to a critical value τ_{c}^{α} (critical shear stress)

$$\forall\ \alpha = 1,\ldots,N_{s}: \quad \begin{cases} |\tau^{\alpha}| < \tau_{c}^{\alpha} \Rightarrow \dot{\gamma}^{\alpha} = 0 \\ |\tau^{\alpha}| = \tau_{c}^{\alpha} \Rightarrow \dot{\gamma}^{\alpha} \geq 0. \end{cases} \tag{14}$$

The evolution of τ_{c}^{α} as a function of $\dot{\gamma}^{\beta}$ is given by the following generic form:

$$\forall\ \alpha = 1,\ldots,N_{s}: \quad \dot{\tau}_{c}^{\alpha} = h^{\alpha\beta}\,\dot{\gamma}^{\beta} \quad ; \quad \beta = 1,\ldots,N_{s}, \tag{15}$$

where $h^{\alpha\beta}$ are the $\alpha\beta$ components of a square matrix $\mathbf{h}$ describing the single crystal hardening.

The slip rates can be computed by using the consistency condition, which is simply the rate form of the Schmid law (14)

$$\forall\ \alpha\in\mathscr{A}: \quad \dot{\chi}^{\alpha} = \operatorname{sgn}(\tau^{\alpha})\,\dot{\tau}^{\alpha} - \dot{\tau}_{c}^{\alpha} = 0, \tag{16}$$

where $\mathscr{A}$ is the set of active slip systems ($\alpha\in\mathscr{A}\Leftrightarrow\dot{\gamma}^{\alpha}>0$).

The combination of Eqs. (13) (15) and (16) yields

$$\forall\ \alpha\in\mathscr{A}: \quad \operatorname{sgn}(\tau^{\alpha})\,\mathbf{R}^{\alpha}\colon\mathbf{l}^{e}\colon\mathbf{d} = \left(h^{\alpha\beta}+\operatorname{sgn}(\tau^{\alpha})\operatorname{sgn}(\tau^{\beta})\,\mathbf{R}^{\alpha}\colon\mathbf{l}^{e}\colon\mathbf{R}^{\beta}\right)\dot{\gamma}^{\beta} \quad ; \quad \beta\in\mathscr{A}. \tag{17}$$

Thus, the slip rates of the different active slip systems finally read

$$\forall\ \alpha\in\mathscr{A}: \quad \dot{\gamma}^{\alpha} = M^{\alpha\beta}\operatorname{sgn}(\tau^{\beta})\,\mathbf{R}^{\beta}\colon\mathbf{l}^{e}\colon\mathbf{d} \quad ; \quad \beta\in\mathscr{A}, \tag{18}$$

with $\mathbf{M}$ being the inverse of matrix $\mathbf{A}$, which is defined by the following index form:

$$\forall\ \alpha,\ \beta\in\mathscr{A}: \quad A^{\alpha\beta} = h^{\alpha\beta}+\operatorname{sgn}(\tau^{\alpha})\operatorname{sgn}(\tau^{\beta})\,\mathbf{R}^{\alpha}\colon\mathbf{l}^{e}\colon\mathbf{R}^{\beta}. \tag{19}$$

The constitutive equation for the single crystal relates the velocity gradient $\mathbf{g}$ to the nominal stress rate $\dot{\mathbf{n}}$, using the microscopic tangent modulus $\boldsymbol{l}$, as follows:

$$\dot{\mathbf{n}} = \mathbf{l}:\mathbf{g}, \tag{20}$$

where $\dot{\mathbf{n}}$ is defined by the following expression:

$$\dot{\mathbf{n}} = j\,\mathbf{f}^{-1}.(\dot{\boldsymbol{\sigma}}+\boldsymbol{\sigma}\operatorname{Tr}(\mathbf{d})-\mathbf{g}.\boldsymbol{\sigma}), \tag{21}$$

in which j denotes the Jacobian of the deformation gradient $\mathbf{f}$ and $\operatorname{Tr}(\bullet)$ is the trace of tensor $\bullet$. By adopting an updated Lagrangian formulation (i.e., $j=1$ and $\mathbf{f}=\mathbf{I}_2$), Eq. (21) becomes

$$\dot{\mathbf{n}} = \dot{\boldsymbol{\sigma}}+\boldsymbol{\sigma}\operatorname{Tr}(\mathbf{d})-\mathbf{g}.\boldsymbol{\sigma}. \tag{22}$$

Taking Eqs. (6) (10) and (11) into account, $\dot{n}$ can be given by the following expression:

$$\dot{\mathbf{n}} = (\mathbf{l}^{e}+\boldsymbol{\sigma}\otimes\mathbf{I}_2)\colon d-\boldsymbol{\sigma}\,.\,\mathbf{w}-d\,.\,\boldsymbol{\sigma}-\operatorname{sgn}(\tau^{\alpha})\,(\mathbf{l}^{e}\colon\mathbf{R}^{\alpha}+\mathbf{S}^{\alpha}\,.\,\boldsymbol{\sigma}-\boldsymbol{\sigma}\,.\,\mathbf{S}^{\alpha})\,\dot{\gamma}^{\alpha} \quad ; \quad \alpha\in\mathscr{A}. \tag{23}$$

Replacing $\dot{\gamma}^{\alpha}$ in Eq. (23) by its expression from Eq. (18), one obtains the following expression of microscopic tangent modulus $\boldsymbol{l}$:

$$\mathbf{l} = \mathbf{l}^{e}+\boldsymbol{\sigma}\otimes\mathbf{I}_2-{}^{1}_{\sigma}\mathbf{l}-{}^{2}_{\sigma}\mathbf{l}-\operatorname{sgn}(\tau^{\alpha})\operatorname{sgn}(\tau^{\beta})\,M^{\alpha\beta}(\mathbf{l}^{e}\colon\mathbf{R}^{\alpha}+\mathbf{S}^{\alpha}\,.\,\boldsymbol{\sigma}-\boldsymbol{\sigma}\,.\,\mathbf{S}^{\alpha})\otimes\left(\mathbf{R}^{\beta}\colon\mathbf{l}^{e}\right) \quad ; \quad \alpha,\beta\in\mathscr{A}, \tag{24}$$

where symbol '$\otimes$' refers to the tensor product, while ${}^{1}_{\sigma}\mathbf{l}$ and ${}^{2}_{\sigma}\mathbf{l}$ are fourth-order tensors comprising convective terms of the Cauchy stress components. Their index forms are given as follows:

$${}^{1}_{\sigma}\mathbf{l}_{ijkl} = \frac{1}{2}\left(\delta_{jl}\sigma_{ik}-\delta_{jk}\sigma_{il}\right) \quad ; \quad {}^{2}_{\sigma}\mathbf{l}_{ijkl} = \frac{1}{2}\left(\delta_{ik}\sigma_{jl}+\delta_{il}\sigma_{jk}\right), \tag{25}$$

where δ_{jl} denotes the Kronecker delta.

2.2. Numerical integration

The integration of the single crystal constitutive equations is carried out through an implicit incremental algorithm over a typical time interval $[t_n,\ t_{n+1}]$. The material parameters (elasticity and hardening parameters) as well as the mechanical variables γ, τ_c, $\mathbf{h}$, $\mathbf{r}$, and $\boldsymbol{\sigma}$ at t_n are assumed to be known. We also assume that the microscopic velocity gradient $\mathbf{g}$ is known and held constant over $[t_n,\ t_{n+1}]$. The main task of the present algorithm is to numerically determine the values of the variables γ, τ_c, $\mathbf{h}$, $\mathbf{r}$, and $\boldsymbol{\sigma}$ at t_{n+1}. By analyzing the set of constitutive equations at the single crystal scale, it clearly appears that the determination of the set of active slip systems $\mathscr{A}$ and the corresponding slip rates $\dot{\gamma}^{\alpha}$ allows the computation of the value of all other variables at t_{n+1}. The computation of the slip rates for the active slip systems essentially leads to three fundamental problems:

- **The first problem** is related to the determination of the set of potentially active slip systems over $[t_n, t_{n+1}]$. To solve this problem, two main classes of algorithms have been developed in the literature. The first class includes the usual return-

mapping algorithms (see, e.g., Anand and Kothari, 1996; Miehe and Schröder, 2001), where the set of potentially active slip systems is computed at the end of the time increment (i.e., at t_{n+1}):

$$\mathscr{P} = \left\{\alpha = 1, ..., N_s \ : \ |\tau^{\alpha}_{tr}(t_{n+1})| - \tau^{\alpha}_{c}(t_n) \geq 0\right\}, \tag{26}$$

where the resolved shear stress $\tau^{\alpha}_{tr}(t_{n+1})$ used in the return-mapping algorithm represents the trial resolved shear stress.

The second class of integration schemes may be built following the so-called ultimate algorithm, initially introduced by Borja and Wren (1993) and subsequently followed by (Knockaert et al., 2002; Ben Bettaieb et al., 2012), where the set of potentially active slip systems is computed at the beginning of the time increment (i.e., at t_n):

$$\mathscr{P} = \left\{\alpha = 1, ..., N_s \ : \ |\tau^{\alpha}(t_n)| - \tau^{\alpha}_{c}(t_n) \geq 0\right\} \tag{27}$$

The algorithm used in the current paper follows the class of ultimate algorithms, which reveals to be more efficient than the class of return-mapping algorithms (see Akpama et al., 2016).

- **The second problem** concerns the computation of the slip rates for the active slip systems. To compute these slip rates, the consistency condition, reduced to the slip systems belonging to $\mathscr{P}$, should be fulfilled:

$$\forall\ \alpha \in \mathscr{P} : \quad \chi^{\alpha} = \text{sgn}\,(\tau^{\alpha})\,\tau^{\alpha} - \tau^{\alpha}_{c} \leq 0 \quad ; \quad \dot{\gamma}^{\alpha} \geq 0 \quad ; \quad \chi^{\alpha}\,\dot{\gamma}^{\alpha} \ = \ 0. \tag{28}$$

This problem is usually decomposed in the majority of contributions (see, for instance, Anand and Kothari, 1996; Knockaert et al., 2002) into two sub-problems: the identification of the set of active slip systems among the potentially active ones, and the computation of the slip rates for the corresponding active slip systems. To this end, a combinatorial search strategy, very similar to the one used in Anand and Kothari (1996), can be used. This search strategy is carried out iteratively and, at each iteration, a subset of the set of potentially active slip systems is selected to be the set of active slip systems. The slip rate of each presumed active slip system is computed by enforcing the equality between its critical shear stress and its resolved shear stress (i.e., enforcing $\chi^{\alpha} = 0$ in Eq. $(28)_1$). As τ^{α} and τ^{α}_{c} are both dependent on the slip rates of the presumed active slip systems, the constraint $\chi^{\alpha} = 0$ is a non-linear equation, which can be solved by using the fixed point method, for instance, as done in Ben Bettaieb et al. (2012). For the other slip systems, belonging to the set of potentially active slip systems, their slip rates are assumed to be equal to zero. After this step, the consistency condition given by Eq. (28) is checked for all of the potentially active slip systems. If at least one constraint of this consistency condition is violated, then the assumed set is not an effective set of active slip systems and another set is chosen. Several techniques have been used in the literature to select the set of active slip systems for the next search iteration, such as the intuitive combinatorial strategy developed in Ben Bettaieb et al. (2012). Despite its wide use, this combinatorial search strategy has shown its limitations compared to the strategy based on the use of the semi-smooth Fischer–Burmeister function (Fischer, 1992, 1997). Within this latter strategy, the consistency condition given by Eq. (28) may be viewed as a non-smooth complementarity problem, and can therefore be replaced by an equivalent system involving the semi-smooth Fischer–Burmeister function:

$$\forall\ \alpha \in \mathscr{P} : \quad \varphi^{\alpha} \ = \ \sqrt{(\chi^{\alpha})^2 + (\dot{\gamma}^{\alpha})^2} - (\chi^{\alpha} + \dot{\gamma}^{\alpha}) = 0. \tag{29}$$

The above Eq. (29) appears as a system of non-linear equations. The dimension of this system is equal to card($\mathscr{P}$). The slip rates of the potentially active slip systems (and then the set of active slip systems $\mathscr{A}$) can be determined by solving the system of non-linear equation (29) using a global Newton–Raphson method. The components of the corresponding Jacobian matrix **J** are defined by the following relations:

$$\forall\ \alpha, \beta \in \mathscr{P} : \quad J^{\alpha\beta} \ = \left(\frac{\dot{\gamma}^{\alpha}}{\sqrt{(\chi^{\alpha})^2 + (\dot{\gamma}^{\alpha})^2}} - 1\right) \delta^{\alpha\beta} - \left(\frac{\chi^{\alpha}}{\sqrt{(\chi^{\alpha})^2 + (\dot{\gamma}^{\alpha})^2}} + 1\right) A^{\alpha\beta}, \tag{30}$$

where **A** is the matrix introduced in Eq. (19).

The initial guess for the slip rates required at the beginning of the iterative process of each time increment corresponds to the last converged values for these slip rates at the previous increment. At convergence of the Newton–Raphson procedure, the slip rates of some systems belonging to the set $\mathscr{P}$ are found practically equal to zero. These systems are obviously inactive during the current time increment. The slip rates of the other potentially active slip systems are certainly strictly positive.

These latter slip systems constitute the set of active slip systems $\mathscr{A}$. Once the slip rates of the potentially active slip systems calculated, the resolved and the critical shear stresses should be updated (i.e., computed at t_{n+1}). The following inequality should be checked for all of the slip systems:

$$\forall\ \alpha = 1, ..., N_s: \quad |\tau^{\alpha}(t_{n+1})| \leq \tau_c^{\alpha}(t_{n+1}). \tag{31}$$

This inequality is obviously satisfied for the potentially active slip systems. But, occasionally, Eq. (31) may be violated by one or several non-potential slip systems. In such a case, these slip systems must be added to the set of potentially active slip systems, and the proceduredeveloped to solve the system of non-linear equation (29) is repeated until complete fulfillment of inequality (31) for all of the slip systems. The use of the alternative formulation (29) instead of the original one (28) makes it possible to merge two tasks: the determination of the set of active slip systems $\mathscr{A}$, and the calculation of the corresponding slip rates. Such a combination allows significantly increasing the efficiency of the proposed numerical scheme (Akpama et al., 2016). The application of this algorithm always allows the computation of the slip rates of the active slip systems in few iterations (the number of iterations does not typically exceed 3 or 4).

- **The third problem** is related to the possible non-uniqueness of slip rates. This problem may occur, for instance, when the Jacobian matrix **J** used for the application of the Newton–Raphson method becomes singular (Eq. (30)). In such a situation, the solution of the system of equation (29) in terms of slip rates becomes non-unique. To avoid this problem, the pseudo-inversion technique is used in the current paper. This technique, which has been initially used in Anand and Kothari (1996), allows computing the pseudo-inverse of the Jacobian matrix **J**, thus identifying a unique set of slip rates. To investigate the effect of the method adopted for the determination of the set of active slip systems and the corresponding slip rates (when the solution of system (29) is not unique) on the prediction of forming limit diagrams, the results obtained by the application of the pseudo-inversion technique should be confronted to the predictions given by other techniques, such as the perturbation approach, initially introduced in Ben Bettaieb et al. (2012). The authors of the latter paper have demonstrated, through an extensive statistical study, that the mechanical response at the single crystal scale may be highly sensitive to the techniques used to solve the non-uniqueness problem. However, the sensibility of the mechanical response at the polycrystalline scale to these techniques is shown to be very small. Therefore, we believe that the impact of the technique used to determine the slip rates of the active slip systems (when the solution is not unique) on the forming limit diagrams of polycrystalline aggregates is negligible. This idea should be confirmed through an appropriate sensitivity study. This will be the matter (among other points) of future works.

Once the determination of the active slip systems and their slip rates is achieved, all other mechanical variables (vectors $\boldsymbol{\gamma}$ and $\boldsymbol{\tau}_c$, matrix **h**, and tensors **r** and $\boldsymbol{\sigma}$) can be updated by using the Euler backward integration scheme. Finally, the microscopic tangent modulus **l** is evaluated at t_{n+1} by using Eq. (24).

3. Polycrystal modeling

3.1. Theoretical framework

In the current study, the self-consistent multi-scale model developed in Lipinski and Berveiller (1989) is adopted. To be brief, only the main lines of this approach are provided in this paper.

Similar to the single crystal behavior law (Eq. (20)), a relation between the macroscopic velocity gradient **G** and the macroscopic nominal stress rate $\dot{\mathbf{N}}$, using the macroscopic tangent modulus **L**, is sought

$$\dot{\mathbf{N}} = \mathbf{L}\colon \mathbf{G}. \tag{32}$$

On the other hand, $\dot{\mathbf{N}}$ and **G** are related to their microscopic counterparts, namely $\dot{\mathbf{n}}(\mathbf{y})$ and $\mathbf{g}(\mathbf{y})$, respectively, by the following volume average relations (Lipinski and Berveiller, 1989):

$$\dot{\mathbf{N}} = \frac{1}{\Omega}\int_{\Omega} \dot{\mathbf{n}}(\mathbf{y})\, d\mathbf{y} = \langle \dot{\mathbf{n}}(\mathbf{y}) \rangle \quad ; \quad \mathbf{G} = \frac{1}{\Omega}\int_{\Omega} \mathbf{g}(\mathbf{y})\, d\mathbf{y} = \langle \mathbf{g}(\mathbf{y}) \rangle, \tag{33}$$

where Ω denotes the representative volume of the studied polycrystalline aggregate, $\dot{\mathbf{n}}(\mathbf{y})$ and $\mathbf{g}(\mathbf{y})$ are the values of $\dot{\mathbf{n}}$ and **g**, respectively, at the material point **y**, while $\langle \bullet \rangle$ refers to the weighted average of a given field $\bullet$ over the representative volume Ω.

Furthermore, the microscopic velocity gradient $\mathbf{g}(\mathbf{y})$ can be related to the macroscopic one **G** via a fourth-order concentration tensor denoted $\mathbf{A}(\mathbf{y})$.

$$\mathbf{g}(\mathbf{y}) = \mathbf{A}(\mathbf{y}) : \mathbf{G}. \tag{34}$$

By introducing the expression of $\mathbf{g}(\mathbf{y})$, given by Eq. (34), into the microscopic behavior law (20), and using the average relations of Eq. $(33)_1$, we can easily deduce the following expression for the macroscopic tangent modulus $\mathbf{L}$:

$$\mathbf{L} \;=\; \frac{1}{\Omega}\int_{\Omega} \mathbf{l}(\mathbf{y}) : \mathbf{A}(\mathbf{y})\, \mathrm{d}\mathbf{y} \;=\; \langle \mathbf{l}(\mathbf{y}) : \mathbf{A}(\mathbf{y}) \rangle. \tag{35}$$

From Eq. (35), it is clear that the unknown variable required for the determination of $\mathbf{L}$ is the concentration tensor $\mathbf{A}(\mathbf{y})$. Unfortunately, the analytical expression of $\mathbf{A}(\mathbf{y})$ is difficult to derive explicitly. Nevertheless, it can be approximated after solving the following integral equation involving the velocity gradient (Lipinski and Berveiller, 1989):

$$\mathbf{g}(\mathbf{y}) = \mathbf{g}_0 + \int_{\Omega} \mathbf{\Gamma}(\mathbf{y}-\mathbf{y}') \Big(\mathbf{l}(\mathbf{y}') - \mathbf{L}^{\,0} \Big) : \mathbf{g}(\mathbf{y}')\, \mathrm{d}\mathbf{y}', \tag{36}$$

where $\mathbf{g}_0$ is the velocity gradient of a reference homogeneous medium, $\mathbf{L}^{\,0}$ is the corresponding tangent modulus, and $\mathbf{\Gamma}$ is the fourth-order modified Green tensor. Note that Eq. (36) is the result of the quasi-static equilibrium equation, combined with the boundary conditions on Ω and the constitutive relation of the single crystal (see Eq. (20)).

The self-consistent concept, which is more suited to polycrystalline aggregates, states that the surrounding medium for a given single crystal has the same properties as the effective medium. In other words, the effective medium is chosen to be the same as the reference one

$$\mathbf{L} \;=\; \mathbf{L}^{0}. \tag{37}$$

Furthermore, in order to simplify the integral equation, the assumption of homogeneous deformation inside the grains is made. Accordingly, if we introduce the indicator function $\theta^{\mathrm{I}}(\mathbf{y})$ defined as

$$\begin{cases} \theta^{\mathrm{I}}(\mathbf{y}) = 1 \quad \text{if} \quad \mathbf{y} \in \Omega^{\mathrm{I}} \\ \theta^{\mathrm{I}}(\mathbf{y}) = \;\; 0 \quad \text{if} \quad \mathbf{y} \notin \Omega^{\mathrm{I}} \end{cases}, \tag{38}$$

then

$$\mathbf{g}(\mathbf{y}) = \mathbf{g}^{\mathrm{I}}\, \theta^{\mathrm{I}}(\mathbf{y}) \quad ; \quad \mathbf{l}(\mathbf{y}) = \mathbf{l}^{\mathrm{I}}\, \theta^{\mathrm{I}}(\mathbf{y}) \quad ; \quad \mathrm{I} = 1, \ldots, \mathrm{N_g}, \tag{39}$$

where Ω^{I} denotes the volume of grain I and $\mathrm{N_g}$ the number of grains that make up the polycrystal.

With the above relations, Eq. (36) can be rewritten as follows:

$$\mathbf{g} \;=\; \mathbf{g}_0 + \mathbf{T}^{\mathrm{II}} : (\mathbf{l}^{\mathrm{I}} - \mathbf{L}) : \mathbf{g}^{\mathrm{I}} + \sum_{\mathrm{J} \neq \mathrm{I}} \mathbf{T}^{\mathrm{IJ}} \colon (\mathbf{l}^{\mathrm{I}} - \mathbf{L}) : \mathbf{g}^{\mathrm{J}}, \tag{40}$$

where $\mathbf{T}^{\mathrm{IJ}}$ is a fourth-order tensor that represents the interaction between grains I and J. This interaction tensor is defined as

$$\mathbf{T}^{\mathrm{IJ}} = \frac{1}{\Omega^{\mathrm{I}}} \int_{\Omega^{\mathrm{I}}} \int_{\Omega^{\mathrm{J}}} \mathbf{\Gamma}(\mathbf{y}-\mathbf{y}')\, \mathrm{d}\mathbf{y}\, \mathrm{d}\mathbf{y}'. \tag{41}$$

For $\mathrm{I} = \mathrm{J}$, $\mathbf{T}^{\mathrm{II}}$ represents the interaction between grain I and the reference medium.

Because the effective medium is taken to be the same as the reference one, the interaction between two grains is negligible compared to the interaction between a grain and the reference medium (since this reference medium already accounts for the contribution of all other grains). In other words, the sum $\sum_{\mathrm{J} \neq \mathrm{I}} \mathbf{T}^{\mathrm{IJ}} \colon (\mathbf{l}^{\mathrm{J}} - \mathbf{L}) \colon \mathbf{g}^{\mathrm{J}}$ in Eq. (40) can be ignored compared to $\mathbf{T}^{\mathrm{II}} : (\mathbf{l}^{\mathrm{I}} - \mathbf{L}) : \mathbf{g}^{\mathrm{I}}$. Consequently, Eq. (40) leads to the following relation:

$$\mathbf{g}^{\mathrm{I}} = \Big(\mathbf{I}_4 - \mathbf{T}^{\mathrm{II}} \colon \Big(\mathbf{l}^{\mathrm{I}} - \mathbf{L} \Big) \Big)^{-1} \colon \mathbf{g}_0 \;=\; \mathbf{a}^{\mathrm{I}} \colon \mathbf{g}_0, \tag{42}$$

where $\mathbf{I}_4$ denotes the fourth-order identity tensor.

From Eq. (42), it is possible to express $\mathbf{g}_0$ in terms of $\mathbf{G}$ in order to determine the expression of the fourth-order concentration tensor $\mathbf{A}^{\mathrm{I}}$ associated with grain I. The latter reads

$$\begin{aligned}&\mathbf{g}^{I} = \mathbf{a}^{I}\colon \mathbf{g}_0 \Rightarrow \mathbf{G} = \langle \mathbf{a}^{I} \rangle \colon \mathbf{g}_0 \Rightarrow \mathbf{g}^{I} = \mathbf{a}^{I}\colon \langle \mathbf{a}^{I} \rangle^{-1} : \mathbf{G} = \mathbf{A}^{I}\colon \mathbf{G} \\ &\mathbf{A}^{I} = \left(\mathbf{I}_4 - \mathbf{T}^{II}\colon (\mathbf{I}^{I} - \mathbf{L})\right)^{-1} : \langle \left(\mathbf{I}_4 - \mathbf{T}^{II} : (\mathbf{I}^{I} - \mathbf{L})\right)^{-1} \rangle^{-1}.\end{aligned} \tag{43}$$

In order to completely determine $\mathbf{A}^{I}$, one needs to compute the interaction tensor $\mathbf{T}^{II}$. The explicit analytical expression of $\mathbf{T}^{II}$ can only be found for isotropic elastic media. For the proposed model, the interaction tensor $\mathbf{T}^{II}$ is computed by resorting to Fourier's transforms (Berveiller et al., 1987) through an integral over an ellipsoid representing the grain I. We can therefore express $\mathbf{T}^{II}$ as a function of $\mathbf{L}$ and the three half-axes a, b and c of the ellipsoid (Berveiller et al., 1987)

$$\mathbf{T}^{II} \equiv f(\mathbf{L}, a, b, c). \tag{44}$$

Under the assumption of homogeneity of the microscopic mechanical fields, Eq. (35), which defines the macroscopic tangent modulus, can be equivalently expressed as

$$\mathbf{L} = f^{I}\ \mathbf{I}^{I}\colon \mathbf{A}^{I} \quad ; \quad I = 1, ..., N_g, \tag{45}$$

where f^{I} designates the volume fraction of the I^{th} grain.

Note that when the concentration tensor $\mathbf{A}^{I}$ is set to the fourth-order identity tensor $\mathbf{I}_4$, the self-consistent scheme is obviously reduced to the Taylor model. In this particular case, Eq. (45) reduces to the following expression:

$$\mathbf{L} = f^{I}\ \mathbf{I}^{I} \quad ; \quad I = 1, ..., N_g. \tag{46}$$

3.2. Numerical integration

The computation of the macroscopic tangent modulus $\mathbf{L}$ at the end of a typical time interval $[t_n,\ t_{n+1}]$ is based on the self-consistent approach. The expression of $\mathbf{L}$ presented in Section 3.1 (Eq. (45)) reveals an implicit character, because $\mathbf{A}^{I}$ depends on $\mathbf{L}$ through the expression of $\mathbf{T}^{II}$ and $(\mathbf{I}^{I} - \mathbf{L})$ (see Eq. $(43)_2$). Therefore, the iterative fixed point method is used to compute $\mathbf{L}$. This iterative process is briefly described below:

- Step 1: compute the sth iteration $\mathbf{T}^{II\,(s)}$ (where tensor $\mathbf{T}^{II}$ is defined by Eq. (44)) by using $\mathbf{L}^{(s)}$.
- Step 2: compute $\mathbf{A}^{I\,(s)}$ and $\mathbf{g}^{I\,(s)}$ expressed in Eq. (43).
- Step 3: compute $\boldsymbol{l}^{I\,(s)}$, for each grain I, by integrating the constitutive equations at the single crystal scale (see Section 2.2).
- Step 4: compute the $(s+1)^{th}$ iteration $\mathbf{L}^{(s+1)}$ of $\mathbf{L}$ by using Eq. (45).

The convergence of the iterative procedure defined by Steps $1 \rightarrow 4$ is achieved when the relative difference between two successive iterations of $\mathbf{L}$ becomes smaller than 10^{-3}. The microscopic as well as the macroscopic variables are updated once the convergence of the above fixed point method is reached. As explained in the introduction, the convergence of the fixed point method is not always guaranteed. Consequently, a new algorithm (alternative to the fixed point method), based on the Newton–Raphson method, is developed here to solve the self-consistent equations. This new algorithm is used when the fixed point method fails to converge. The main lines of this new algorithm are given in Appendix A.

4. Strain localization modeling

4.1. Theoretical framework

4.1.1. Plane stress condition and 2D constitutive law

We consider here a thin sheet metal subjected to biaxial loading. We define an orthonormal frame $(\vec{\mathbf{x}}_1,\ \vec{\mathbf{x}}_2,\ \vec{\mathbf{x}}_3)$, which is tied to the sheet (Fig. 2). The axes $\vec{\mathbf{x}}_1$, $\vec{\mathbf{x}}_2$ and $\vec{\mathbf{x}}_3$ coincide with the rolling, transverse, and normal directions of the sheet, respectively.

The studied metal sheet is assumed to be sufficiently thin and, consequently, the plane stress assumption is considered in both localization criteria (namely the bifurcation approach and the M–K analysis). These plane stress conditions are generally expressed by the following relations, which involve the out-of-plane components of the macroscopic Cauchy stress tensor $\boldsymbol{\Sigma}$ (see Fig. 2)

$$\boldsymbol{\Sigma}.\ \vec{\mathbf{x}}_3 = \vec{\mathbf{0}} \quad \Leftrightarrow \quad \Sigma_{13} = \Sigma_{23} = \Sigma_{33} = 0. \tag{47}$$

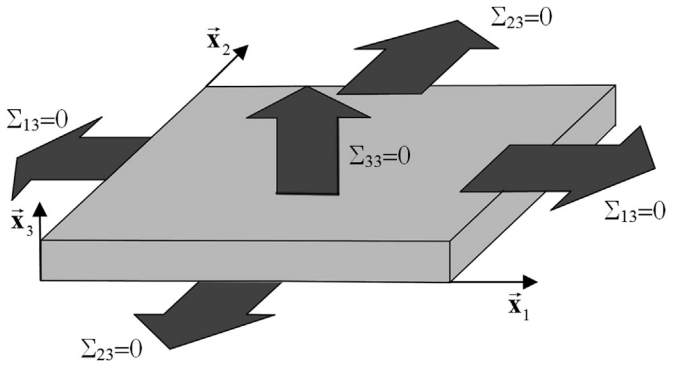

Fig. 2. Metal sheet subjected to plane stress state.

The current work is restricted to orthotropic materials. For this kind of materials, the plane stress condition implies that the following normal components of the macroscopic velocity gradient are equal to zero (Yoshida and Kuroda, 2012; Tadano et al., 2013):

$$G_{13} = G_{31} = G_{23} = G_{32} = 0. \tag{48}$$

Unlike the above-cited references, the polycrystal constitutive equations are formulated here via a relation between the macroscopic velocity gradient $\mathbf{G}$ and the macroscopic nominal stress rate tensor $\dot{\mathbf{N}}$. Consequently, instead of Eq. (47), the plane stress condition can be reformulated as follows:

$$\dot{N}_{13} = \dot{N}_{31} = \dot{N}_{23} = \dot{N}_{32} = \dot{N}_{33} = 0. \tag{49}$$

Using Eq. (32) along with the last equality in Eq. (49) (i.e., $\dot{N}_{33} = 0$), one can derive the expression of the component G_{33} of the macroscopic velocity gradient in terms of its in-plane components $G_{\gamma\delta}$ ($\gamma, \delta = 1,\ 2$).

$$G_{33} = -\frac{L_{33\gamma\delta}}{L_{3333}}\ G_{\gamma\delta} \quad ; \quad \gamma, \delta = 1, 2. \tag{50}$$

By inserting Eq. (50) into Eq. (32), the following 2D constitutive relation for the polycrystal can be obtained:

$$\forall \alpha, \beta = 1, 2: \quad \dot{N}_{\alpha\beta} = \left[L_{\alpha\beta\gamma\delta} - \frac{L_{\alpha\beta33}\ L_{33\gamma\delta}}{L_{3333}}\right]\ G_{\gamma\delta} \quad ; \quad \gamma, \delta = 1, 2. \tag{51}$$

To simplify the notations, Eq. (51) can be expressed in the following generic tensor form:

$$\dot{\mathbf{N}}^{PS} = \mathbf{L}^{PS} : \mathbf{G}^{PS}, \tag{52}$$

where $\bullet^{PS}$ denotes the in-plane part of second-order tensor or vector $\bullet$ defined as $\begin{pmatrix} \bullet_{11} & \bullet_{12} \\ \bullet_{21} & \bullet_{22} \end{pmatrix}$ or $(\bullet_1 \quad \bullet_2)$, respectively.

4.1.2. Bifurcation theory

We consider a homogeneous sheet metal subjected to a uniform deformation state. To predict the onset of strain localization, the bifurcation theory is applied. This bifurcation phenomenon corresponds to the loss of uniqueness for the solution to the rate equilibrium equations. The onset of bifurcation is associated with the emergence of a non-uniform deformation mode through the sheet. This non-uniformity manifests itself as a planar localization band, which remains normal to the plane of the sheet during deformation. Accordingly, the unit vector $\overrightarrow{\mathcal{N}}^{PS} = (\cos\theta,\ \sin\theta)$, normal to the localization band, is restricted to rotate in the sheet plane (see Fig. 3). In other words, the associated bifurcation problem is taken to be two-dimensional, whereby the sheet undergoes plane stress conditions. As illustrated in Fig. 3, the in-plane velocity gradient outside (resp. inside) the band is denoted by $\mathbf{G}^{PS\ H}$ (resp. $\mathbf{G}^{PS\ B}$), while the corresponding nominal stress rate is denoted by $\dot{\mathbf{N}}^{PS\ H}$ (resp. $\dot{\mathbf{N}}^{PS\ B}$).

The equilibrium condition between the band and the homogeneous zone (called also the safe zone) can be expressed as follows:

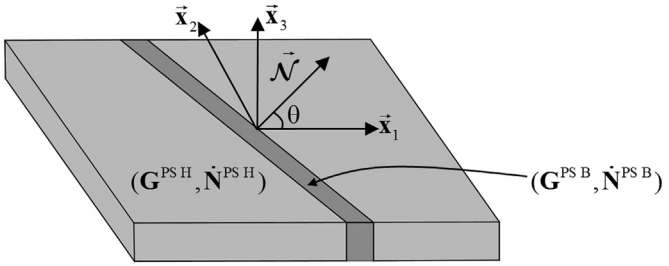

Fig. 3. Illustration of the localization bifurcation phenomenon in a thin sheet metal.

$$\overrightarrow{\mathcal{N}}^{PS} . [\![\dot{\mathbf{N}}^{PS}]\!] = \vec{\mathbf{0}}, \tag{53}$$

where $[\![\bullet]\!] = \bullet^{B} - \bullet^{H}$ denotes the jump in a tensor field $\bullet$ across the band.

Maxwell's theorem requires that the jump in the velocity gradient $\mathbf{G}^{PS}$ through the discontinuity surface be equal to the tensor product of a given vector $\dot{\vec{\mathbf{C}}}^{PS}$ (referred to as the jump vector) and the normal $\overrightarrow{\mathcal{N}}^{PS}$ to the localization band

$$[\![\mathbf{G}^{PS}]\!] = \dot{\vec{\mathbf{C}}}^{PS} \otimes \overrightarrow{\mathcal{N}}^{PS}. \tag{54}$$

The combination of Eqs. (53) and (54) along with the 2D constitutive equation (52) yields

$$\overrightarrow{\mathcal{N}}^{PS} . \left(\mathbf{L}^{PS\ H} : \left(\dot{\vec{\mathbf{C}}}^{PS} \otimes \overrightarrow{\mathcal{N}}^{PS} \right) \right) = \overrightarrow{\mathcal{N}}^{PS} . \left(\left(\mathbf{L}^{PS\ H} - \mathbf{L}^{PS\ B} \right) : G^{PS\ B} \right). \tag{55}$$

If one assumes that, at the inception of bifurcation, the tangent modulus $\mathbf{L}^{PS}$ is continuous across the band (i.e., $[\![\mathbf{L}^{PS}]\!] = \mathbf{L}^{PS\ B} - \mathbf{L}^{PS\ H} = \mathbf{0}$), then Eq. (55) gives

$$\left(\overrightarrow{\mathcal{N}}^{PS} . \mathbf{L}^{PS\ H} . \overrightarrow{\mathcal{N}}^{PS} \right) . \dot{\vec{\mathbf{C}}}^{PS} = \vec{0}. \tag{56}$$

As long as the so-called 2D acoustic tensor $\overrightarrow{\mathcal{N}}^{PS} . \mathbf{L}^{PS\ H} . \overrightarrow{\mathcal{N}}^{PS}$ is invertible, one obtains a trivial jump vector $\dot{\vec{\mathbf{C}}}^{PS}$, whose components are all equal to zero, and, hence, the deformation remains uniform. When the tensor $\overrightarrow{\mathcal{N}}^{PS} . \mathbf{L}^{PS\ H} . \overrightarrow{\mathcal{N}}^{PS}$ becomes singular, there is an infinity of jump vectors that satisfy Eq. (56). This singularity condition is physically interpreted as the occurrence of effective bifurcation, which marks the onset of strain localization

$$\det \left(\overrightarrow{\mathcal{N}}^{PS} . \mathbf{L}^{PS\ H} . \overrightarrow{\mathcal{N}}^{PS} \right) = 0. \tag{57}$$

This criterion is often referred to as the Rice bifurcation criterion (Rice, 1976).

4.1.3. Initial imperfection analysis

This approach, initially introduced by Marciniak and Kuczynski (1967), is also known as the M–K analysis. It relies on the assumption of the preexistence of an initial geometric defect in the form of a band along the width of the sheet metal (Fig. 4). Similar to the bifurcation theory, mechanical fields inside (resp. outside) the band are referred to by the exponent B (resp. H).

The current thickness e^{B} (resp. e^{H}) is expressed as a function of its initial value e_0^{B} (resp. e_0^{H}) by the following relations:

$$e^{H} = e_0^{H} \exp(E_{33}^{H}) \quad ; \quad e^{B} = e_0^{B} \exp(E_{33}^{B}), \tag{58}$$

where E_{33}^{H} and E_{33}^{B} are, respectively, the logarithmic strains outside and inside the band in the direction normal to the sheet.

According to the notations adopted in Fig. 4, the initial (resp. current) geometric imperfection may be measured by a ratio ξ_0 (resp. ξ) defined as

$$\xi_0 = 1 - \frac{e_0^{B}}{e_0^{H}} \quad ; \quad \xi = 1 - \frac{e^{B}}{e^{H}}. \tag{59}$$

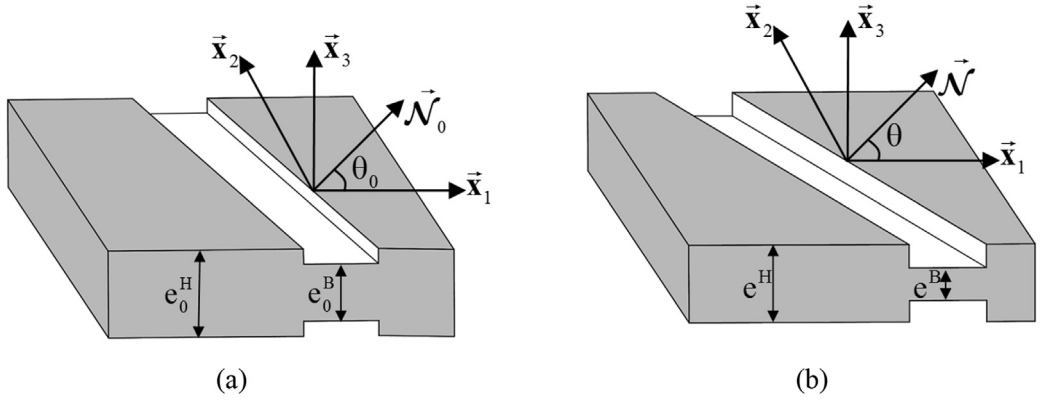

Fig. 4. Illustration of the initial imperfection analysis: (a) Initial configuration of the sheet; (b) Current configuration of the sheet.

This initial (resp. current) imperfection is also characterized by the orientation θ_0 (resp. θ) of the normal vector $\overrightarrow{\mathcal{N}}_0^{PS}$ (resp. $\overrightarrow{\mathcal{N}}^{PS}$) with respect to the major strain direction. The evolution law for the band orientation θ involves three quantities: the initial band orientation θ_0, the logarithmic strain outside the band along the rolling direction E_{11}^H, and the strain-path parameter ρ defined as the ratio G_{22}^H/G_{11}^H:

$$\theta = \arctan\left[\tan\theta_0 \ \exp\left(1-\rho\right) \ E_{11}^H\right]. \tag{60}$$

In addition to Eqs. (58)–(60), the initial imperfection approach is defined by the following relations:

- The kinematic compatibility condition at the interface between the homogeneous zone and the band, which is similar to Eq. (54) involved in the case of bifurcation theory:

$$\mathbf{G}^{PS\ B} = \mathbf{G}^{PS\ H} + \dot{\overrightarrow{\mathbf{C}}}^{PS} \otimes \overrightarrow{\mathcal{N}}^{PS}. \tag{61}$$

- The equilibrium equation across the interface between the homogeneous zone and the geometric defect in the form of a groove:

$$e^B \, \mathbf{\Sigma}^{PS\ B}.\overrightarrow{\mathcal{N}}^{PS} = e^H \, \mathbf{\Sigma}^{PS\ H}.\overrightarrow{\mathcal{N}}^{PS}, \tag{62}$$

which is equivalent to the following rate form:

$$e^B \overrightarrow{\mathcal{N}}^{PS}.\dot{\mathbf{N}}^{PS\ B} = e^H \overrightarrow{\mathcal{N}}^{PS}.\dot{\mathbf{N}}^{PS\ H}. \tag{63}$$

Eq. (63) is more suitable to the macroscopic constitutive relations developed in the present paper.

- The 2D constitutive relations developed in Section 4.1.1, expressed inside and outside the band, respectively:

$$\dot{\mathbf{N}}^{PS\ B} = \mathbf{L}^{PS\ B} : \mathbf{G}^{PS\ B} \quad ; \quad \dot{\mathbf{N}}^{PS\ H} = \mathbf{L}^{PS\ H} : \mathbf{G}^{PS\ H}. \tag{64}$$

Using Eq. (64), the equilibrium condition (63) can be equivalently rewritten as a function of $\mathbf{G}^{PS\ B}$, $\mathbf{G}^{PS\ H}$ and the tangent moduli $\mathbf{L}^{PS\ B}$ and $\mathbf{L}^{PS\ H}$. Then, the compatibility condition (61) can be used to compute the jump vector $\dot{\overrightarrow{\mathbf{C}}}^{PS}$.

$$\left(\overrightarrow{\mathcal{N}}^{PS}.\mathbf{L}^{PS\ B}.\overrightarrow{\mathcal{N}}^{PS}\right).\dot{\overrightarrow{\mathbf{C}}}^{PS} = \overrightarrow{\mathcal{N}}^{PS}.\left[\left(\frac{e^H}{e^B}\mathbf{L}^{PS\ H} - \mathbf{L}^{PS\ B}\right) : \mathbf{G}^{PS\ H}\right], \tag{65}$$

which is equivalent to

$$\dot{\overrightarrow{\mathbf{C}}}^{PS} = \left(\overrightarrow{\mathscr{N}}^{PS} . \mathbf{L}^{PS\ B} . \overrightarrow{\mathscr{N}}^{PS}\right)^{-1} . \left[\overrightarrow{\mathscr{N}}^{PS} . \left[\left(\frac{e^{H}}{e^{B}} \mathbf{L}^{PS\ H} - \mathbf{L}^{PS\ B}\right) : \mathbf{G}^{PS\ H}\right]\right]. \tag{66}$$

A natural outcome from Eq. (66) is that $\dot{\overrightarrow{C}}^{PS}$ becomes unbounded when the 2D acoustic tensor in the band approaches singularity (i.e., its determinant is close to zero)

$$\left\|\dot{\overrightarrow{\mathbf{C}}}^{PS}\right\| \to \infty \quad \Leftrightarrow \quad \det\left(\overrightarrow{\mathscr{N}}^{PS} . \mathbf{L}^{PS\ B} . \overrightarrow{\mathscr{N}}^{PS}\right) = 0. \tag{67}$$

Furthermore, in the limiting case of a very small size for the initial geometric defect, e_0^B is very close to e_0^H. In such a situation, it is legitimate to suppose that, before the occurrence of localized necking, the mechanical variables inside the band evolve but remain essentially equal to their counterparts outside the band. Consequently, Eq. (65) is approximately equivalent to

$$\left(\overrightarrow{\mathscr{N}}^{PS} . \mathbf{L}^{PS\ B} . \overrightarrow{\mathscr{N}}^{PS}\right) . \dot{\overrightarrow{\mathbf{C}}}^{PS} = \overrightarrow{0}. \tag{68}$$

Comparing the above Eq. (68) with the bifurcation criterion (56), it is reasonable to expect that the limit strains predicted by the initial imperfection approach tend to those obtained by the bifurcation theory when ξ_0 (see Eq. $(59)_1$) tends towards zero. This key issue has been discussed in the literature for phenomenological models (Abed-Meraim et al., 2014; Ben Bettaieb and Abed-Meraim, 2015). In the context of micromechanical modeling, this fundamental comparison between bifurcation and M−K analysis will be extensively studied in Section 5 for the multi-scale model developed in the current paper.

4.2. Numerical integration

4.2.1. Adaptation of the mechanical problem to the plane stress state

The numerical method adopted to apply the plane stress conditions should be first explained. Under plane stress conditions, tensors $\mathbf{G}$ and $\dot{\mathbf{N}}$ can be defined by the following generic expressions:

$$\mathbf{G} = \begin{pmatrix} G_{11} & G_{12} & 0 \\ G_{21} & G_{22} & 0 \\ 0 & 0 & ? \end{pmatrix} \quad ; \quad \dot{\mathbf{N}} = \begin{pmatrix} ? & ? & 0 \\ ? & ? & 0 \\ 0 & 0 & 0 \end{pmatrix} \tag{69}$$

The unknown components for both tensors in Eq. (69), which are denoted by symbol ?, should be determined. To this end, the fixed point iterative method is used, which is defined by the following main steps (for a given sth iteration):

- Step 1: use the sth iteration $G_{33}^{(s)}$ to complete $\mathbf{G}^{(s)}$.
- Step 2: compute $\mathbf{L}^{(s)}$ by using the algorithm of Section 3.2. The main input for this algorithm is $\mathbf{G}^{(s)}$, which is determined in Step 1.
- Step 3: compute $G_{33}^{(s+1)}$ by using Eq. (50).

The convergence of the above iterative procedure is achieved when the relative difference between two successive iterations of G_{33}^{B}/G_{33}^{H} becomes smaller than 10^{-3}. Once this iterative process has converged, $\mathbf{L}^{PS}$ is extracted from $\mathbf{L}^{(s)}$ by using Eqs. (51) and (52).

4.2.2. Bifurcation approach

To numerically predict FLDs, the sheet is subjected to proportional loadings with constant strain-path ratios ρ. Before the initiation of plastic strain localization, the sheet is assumed to be homogeneous and, hence, there is no distinction between the band and the homogeneous zone. In this case, the 3D macroscopic velocity gradient $\mathbf{G}$ is obviously homogeneous over the sheet, with no distinction between $\mathbf{G}^{H}$ and $\mathbf{G}^{B}$. The mixed boundary conditions of Eq. (69) are applied with the following additional conditions on the components of $\mathbf{G}$:

$$G_{22} = \rho\ G_{11} \quad ; \quad G_{12} = \ G_{21} = 0. \tag{70}$$

The algorithm for the FLD prediction based on the bifurcation approach relies on two nested loops:

- For each strain path ρ ranging from −0.5 to 1 (with typical intervals of 0.1).
  - For each time interval $[t_n,\ t_{n+1}]$:
    - ✓ Compute $\mathbf{L}^{PS}$ by using the iterative scheme of Section 4.2.1.
    - ✓ For $\theta = 0^\circ$ to 90° at user-defined intervals (with typical increments of 1.5°):

- Compute $\overrightarrow{\mathcal{N}}^{PS} . \mathbf{L}^{PS} . \overrightarrow{\mathcal{N}}^{PS}$.
- Search for $\overrightarrow{\mathcal{N}}^{PS}_{min}$ providing the minimum value for det $(\overrightarrow{\mathcal{N}}^{PS} . \mathbf{L}^{PS} . \overrightarrow{\mathcal{N}}^{PS})$ over the different values of θ.

✓ If det $(\overrightarrow{\mathcal{N}}^{PS}_{min} . \mathbf{L}^{PS} . \overrightarrow{\mathcal{N}}^{PS}_{min}) \leq 0$, then localized necking is detected. The corresponding angle θ is the orientation of the localization band, while the corresponding principal logarithmic strain is the predicted limit strain E_{11}. The computation is then stopped. Otherwise, the integration is continued for the next time increment.

It is worth noting that the range of possible band orientations is restricted to the interval $[0°, 90°]$ because of the symmetry of $\overrightarrow{\mathcal{N}}^{PS} . \mathbf{L}^{PS} . \overrightarrow{\mathcal{N}}^{PS}$ with respect to $\overrightarrow{\mathcal{N}}^{PS}$ as well as the orthotropy properties of the sheet.

4.2.3. Initial imperfection analysis

In the initial imperfection analysis, the mixed boundary conditions applied to the homogeneous zone are the same as those of the bifurcation approach (see Section 4.2.2). The FLD prediction, based on the initial imperfection analysis, is defined by three nested loops:

- For each strain path ρ varying from -0.5 to 1 (with typical intervals of 0.1).

■ For each time increment $[t_n, t_{n+1}]$, use the algorithm of Section 4.2.1 to integrate the constitutive equations of the polycrystalline aggregate representing the homogeneous zone under the plane stress state. The same boundary conditions as those applied in the bifurcation approach (see Section 4.2.2) are used to define the 3D macroscopic velocity gradient $\mathbf{G}^H$. Accordingly, $G^H_{22} = \rho\ G^H_{11}$ and $G^H_{12} = G^H_{21} = 0$. The other components are defined by Eq. (69) developed in Section 4.2.1. The normal vector $\overrightarrow{\mathcal{N}}^{PS}$ is determined at t_{n+1} by using Eq. (60). Vector $\overrightarrow{\mathcal{N}}^{PS}$, tensor $\mathbf{G}^H$, and modulus $\mathbf{L}^{PS\,H}$, computed at t_{n+1}, need to be stored. These quantities will be used hereafter to compute the component G^B_{33} and the jump vector $\overrightarrow{\dot{\mathbf{C}}}^{PS}$, which is given by Eq. (66).

The constitutive equations in the homogeneous zone are incrementally integrated until reaching $E^H_{11} = 1$.

■ For each initial band orientation θ_0 varying from 0° to 90° (with typical increments of 1.5°).

➢ For each time increment $[t_n, t_{n+1}]$:

- Use the values of $\overrightarrow{\mathcal{N}}^{PS}$, $\mathbf{G}^H$ and $\mathbf{L}^{PS\,H}$ evaluated at t_{n+1} to compute the component G^B_{33} and the two components of the jump vector $\overrightarrow{\dot{\mathbf{C}}}^{PS}$. For the sake of clarity, the detailed description of the steps followed to achieve this task is given in a separate section (Section 4.2.4).
- Check the following condition:

$$\left\| \overrightarrow{\dot{\mathbf{C}}}^{PS} \right\| \geq 10. \tag{71}$$

If condition (71) is satisfied, then the logarithmic strain component E^H_{11} is recorded as the critical strain E^*_{11}, corresponding to the initial orientation θ_0. In this case, the computation is stopped. Otherwise, the next time increment is applied.

■ The smallest critical strain E^*_{11} over all initial orientations, and the corresponding initial orientation θ_0 (resp. the corresponding current band orientation) define, respectively, the localization strain E_{11} and the initial localization band orientation θ^L_0 (resp. the current localization band orientation θ^L), corresponding to the current strain-path ratio ρ.

Considering the above algorithm developed for the initial imperfection approach, one can estimate that the incremental integration scheme corresponding to the self-consistent model needs to be called approximatively 2000 times to construct a complete FLD. Indeed, the range of strain paths is discretized with typical intervals of 0.1. Hence, 16 strain paths are simulated to build a complete FLD. For each strain path, the initial band orientation is varied between 0° and 90°, with typical intervals of 1.5°. For each combination of strain path and initial band orientation, the equations governing the mechanical behavior in the band and in the homogeneous zone need to be incrementally solved (until the occurrence of localization), by using the numerical scheme developed for the integration of the equations corresponding to the multiscale scheme. Therefore, it is of utmost importance that the CPU time required for the integration of the equations governing the self-consistent approach be optimized to obtain FLDs within reasonable running times.

4.2.4. Computation of G^B_{33} and $\overrightarrow{\dot{\mathbf{C}}}^{PS}$

The iterative fixed point method is employed to compute G^B_{33} and $\overrightarrow{\dot{\mathbf{C}}}^{PS}$. To this end, the following main steps are required (for a given sth iteration):

into

- Step 1: insert E_{33}^{H} (equal to $E_{33}^{H}(t_n) + (t_{n+1} - t_n)\, G_{33}^{H}$) and $E_{33}^{B\,(s)}$ (equal to $E_{33}^{B}(t_n) + (t_{n+1} - t_n)\, G_{33}^{B\,(s)}$ Eq. (58) and compute the ratio $e^{H\,(s)}/e^{B\,(s)}$.
- Step 2: compute $\mathbf{L}^{B\,(s)}$ by using the algorithm of Section 3.2. The main input for this algorithm is $\mathbf{G}^{B\,(s)}$. Extract $\mathbf{L}^{PS\,B\,(s)}$ from $\mathbf{L}^{B\,(s)}$ by using Eqs. (51) and (52).
- Step 3: compute $\overset{\cdot}{\overrightarrow{\mathbf{C}}}^{PS\,(s+1)}$ and $\mathbf{G}^{PS\,B\,(s+1)}$ by using Eq. (66) and Eq. (61), respectively. Then, compute $G_{33}^{B\,(s+1)}$ by using Eq. (50).

The convergence of the above iterative procedure is achieved when the relative difference between two successive iterations of $\mathbf{G}^{B}$ becomes smaller than 10^{-3}.

5. Numerical predictions and discussions

Several numerical predictions of FLDs, based on both the bifurcation and M−K criteria, are presented in this section. These FLD predictions are then compared and discussed. For the sake of brevity, the full-constraint Taylor model and the self-consistent averaging scheme will be referred to in what follows as the FC and SC models, respectively. Also, the cross coupling between the localized necking criteria and the polycrystal constitutive models will be referred to as follows: MK−FC, for the combination between the M−K analysis and the FC model; MK−SC, for the combination between the M−K analysis and the SC model; BT−FC for the combination between the bifurcation theory and the FC model; and BT−SC, for the combination between the bifurcation theory and the SC model.

5.1. Material data

At the single crystal scale (FCC crystallographic structure), the following material parameters and constitutive choices will be adopted throughout:

- The Poisson ratio and the Young modulus are set to 0.3 and 210 GPa, respectively.
- It is assumed that the different slip systems have the same initial critical shear stress τ_0, which is taken to be equal to 40 MPa.
- Anisotropy is not accounted for in the description of the material hardening. Indeed, all of the components of the hardening matrix $\mathbf{h}$ are taken to be identical, which read

$$\forall\ \alpha,\beta = 1,\ldots,12: \quad h^{\alpha\beta} = h_0\left(1 + \frac{h_0\,\Gamma}{\tau_0\,n}\right)^{n-1} \quad ; \quad \Gamma = \sum_{\alpha=1}^{N_s}\gamma^{\alpha}, \tag{72}$$

where n is the power-law hardening exponent and h_0 is the initial hardening rate. The values of n and h_0 are set equal to 0.35 and 390 MPa, respectively.

The studied polycrystalline aggregate is composed of 2000 grains. We assume that the initial crystallographic texture of this aggregate is orthotropic. This initial texture is generated following the method proposed by Yoshida and Kuroda (2012) and is displayed in Fig. 5.

For the initial morphology of the grains, the latter are assumed to initially have a spherical form, with identical initial volume fraction. It is noteworthy that the grain morphology and its evolution influence the macroscopic properties of the polycrystalline aggregate only when the SC scheme is applied.

As will be seen in Section 5.2, for this initial crystallographic texture (see Fig. 5), the macroscopicresponses (stress−strain curves) obtained by applying the FC model are essentially the same as thoseyielded by the SC model. Therefore, identifying two different sets of hardening parameters (one foreach multiscale scheme) in order to obtain the same mechanical responses (i.e., stress−strain curves) isnot required in this case.

5.2. Simulation of mechanical tests: comparison between the SC and FC models

In order to compare the numerical predictions yielded by the two above-described scale-transition schemes in the context of simple mechanical tests, an equibiaxial tensile test ($\rho = 1$) is simulated for the polycrystalline aggregate defined in Section 5.1. From Fig. 6a, it appears that the stress component Σ_{11} predicted by the FC model lies a little above that predicted by the SC model, although the associated curves are very close. This observation is in agreement with a number of literature results. Indeed, it is well known that the uniform strain assumption of Taylor (1938) and the uniform stress assumption of Reuss (1929) provide upper and lower bounds, respectively, for the effective flow stress. Hence, the self-consistent model, which accounts for grain interaction effects and local non-uniform deformations, and which represents a more realistic deformation mode in polycrystals, has been shown to estimate a softer overall response for rate-independent polycrystals as compared to the FC Taylor model (Bishop and Hill, 1951; Hutchinson, 1970; Takahashi, 1988; Harren and Asaro, 1989). Furthermore, for

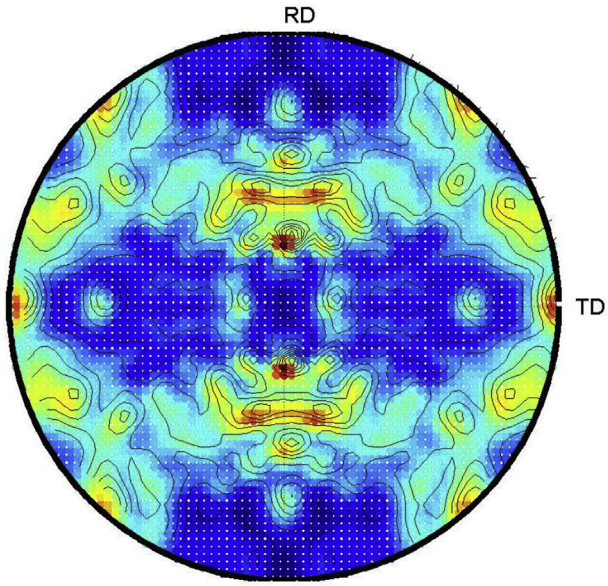

Fig. 5. Initial texture of the studied polycrystalline aggregate: {111} pole figure.

cubic polycrystals (FCC and BCC crystallographic structures) that exhibit high symmetry, Nebozhyn et al. (2001) have demonstrated that, in the context of a viscoplastic formulation, the predictions obtained with the self-consistent scheme tend towards those given by the Taylor model when the rate-sensitivity parameter tends to zero. Harren (1991) also found the same trends by using another variant of the viscoplastic self-consistent model. In Harren's (1991) paper, plane-strain and uniaxial tension have been simulated, in the limit of vanishing rate sensitivity (indeed, the rate-sensitivity parameter has been set to 0.005). In both simulations, the author found that the stress–strain curves predicted by the FC model are consistently higher than those yielded by the SC model. Nevertheless, the stress–strain curves corresponding to these two averaging schemes almost coincide at large strain. In our simulations, which are reported in Fig. 6, similar trends can be observed. The only difference concerns the predictions at small strains. Indeed, unlike Harren's (1991) results, the elastic slope predicted by the SC model (see Fig. 6a) is practically the same as that yielded by the FC model. The main reason to this is that, in our case, the elastic behavior is assumed to be isotropic and therefore independent of grain crystallographic orientations. This is not the case when an orthotropic elastic behavior law is used (Harren, 1991). On the other hand, Fig. 6b shows that the volume average of the number of active slip systems that accommodate the plastic deformation differs from one

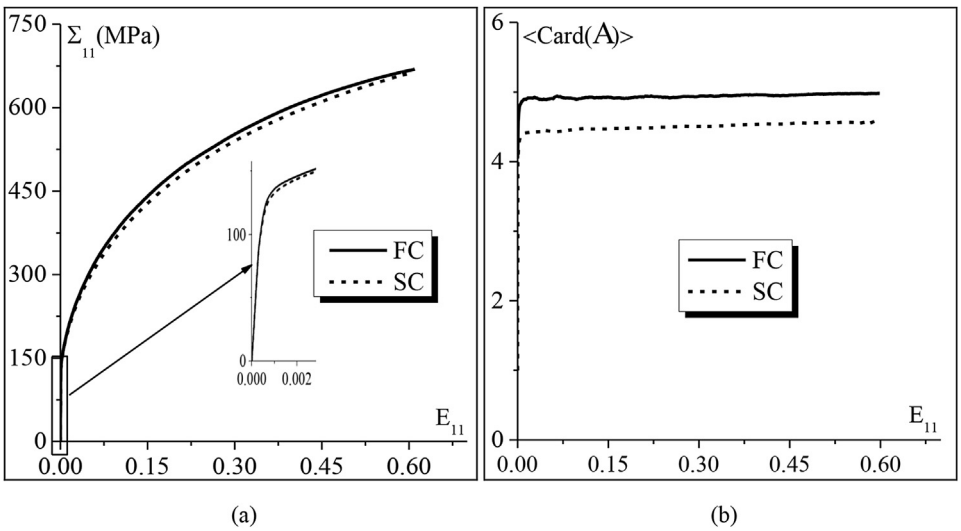

Fig. 6. Simulation of equibiaxial tensile test ($\rho = 1$): (a) Evolution of Σ_{11} as a function of E_{11}; (b) Evolution of the volume average of the number of active slip systems as a function of E_{11}.

scale-transition model to another. Indeed, in the case of the FC model, at large strains, the plastic flow occurs on 4 slip planes for approximately half of the grains that compose the polycrystal, and on 5 slip systems for the other half, whereas for the SC model, the plastic flow occurs on 5 slip systems for most of the grains.

Contrary to the FC model, which is based on uniform deformation, the strain state differs from one grain to another when the SC model is applied. This aspect is illustrated in Fig. 7, where the values (σ_{11}, e_{11}) are displayed for all grains, which represent the component σ_{11} of the microscopic Cauchy stress versus the corresponding component e_{11} of the logarithmic strain. In Fig. 7, these distributions of microscopic stress–strain components are plotted for both scale-transition models, and at two different values of macroscopic strain, namely $E_{11}= 0.2$ and $E_{11}= 0.5$. In the case of the FC model (see Fig. 7a), all grains have the same strain, and only the microscopic stress varies from one grain to another. By contrast, in the case of the SC model (see Fig. 7b), the strain of each grain is determined by its individual velocity gradient. In this latter case, the absolute gap in deformation between the grains increases as the macroscopic strain increases, while the relative gap decreases. Hence, at $E_{11}= 0.2$, the maximal variation in the microscopic strain component e_{11} is approximately equal to 33%, while it is only 26% at $E_{11}= 0.5$. Indeed, in the large strain range, the slip system activity in the grains changes very little, which implies an almost constant interaction relation between the grains and the reference medium, throughout the subsequent deformation. Consequently, the velocity gradient in each grain evolves very slightly, and the absolute deformation gap between the grains increases less than does the amount of strain in the grains.

Fig. 8 compares the crystallographic texture predicted by the FC model to that given by the SC model at a macroscopic strain of $E_{11}= 0.6$. Although they seem to be similar on the whole, they are in fact quite distinct under close examination. Indeed, the texture predicted by the SC model appears to be much sharper than that given by the FC model. As mentioned by Harren (1991), this trend illustrates the fact that the induced anisotropy is better reproduced with the SC model.

5.3. Localized necking predictions

5.3.1. Bifurcation theory

It is now widely recognized that the incremental tangent modulus plays a major role in the determination of the limit strains in the framework of bifurcation theory. Therefore, before applying the bifurcation criterion for predicting the occurrence of plastic flow localization, let us first examine the evolution of the components L_{1111} and L_{1212} of the macroscopic tangent modulus (Fig. 9). The component L_{1111} (resp., L_{1212}) is representative of the non-shearing (resp., shearing) components of the tangent modulus. In Fig. 9, four representative strain paths ($\rho = -0.5$, $\rho = 0$, $\rho = 0.5$, and $\rho = 1$) are used to obtain these evolutions. One can easily observe from Fig. 9 that the evolution of the component L_{1111} is practically the same for both multiscale schemes, especially for the uniaxial tension state ($\rho = -0.5$). However, the evolution of the shearing component L_{1212} differs noticeably from one multiscale scheme to another. In spite of this difference observed in the evolution of L_{1212}, both homogenization schemes lead to the same stress–strain tensile curves (see Fig. 6a). This result is expectable considering the relation that involves the macroscopic Cauchy stress rate $\dot{\boldsymbol{\Sigma}}$, the macroscopic tangent modulus $\mathbf{L}$, and the macroscopic velocity gradient $\mathbf{G}$:

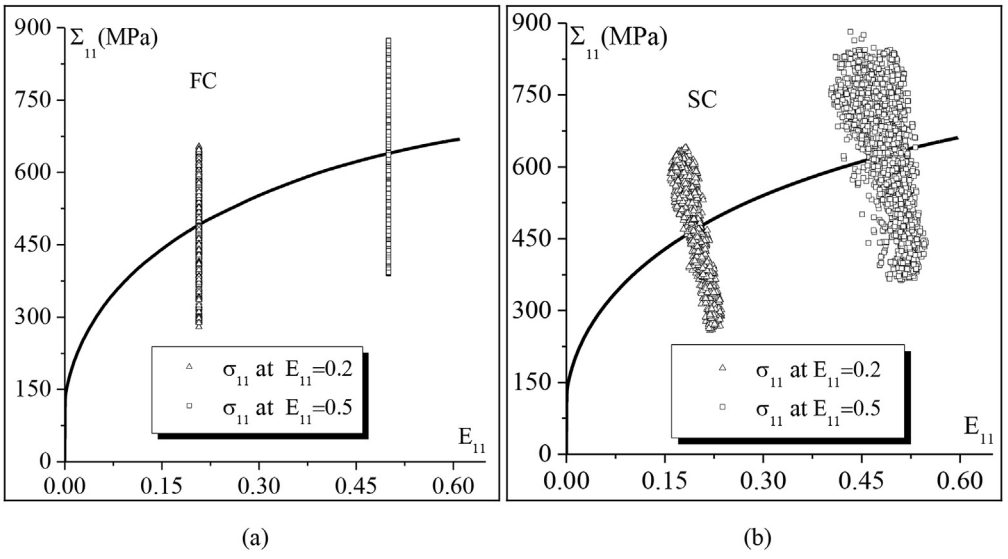

Fig. 7. Distribution of the microscopic stress component σ_{11} and microscopic strain component ε_{11} over the grains: (a) FC model; (b) SC model.

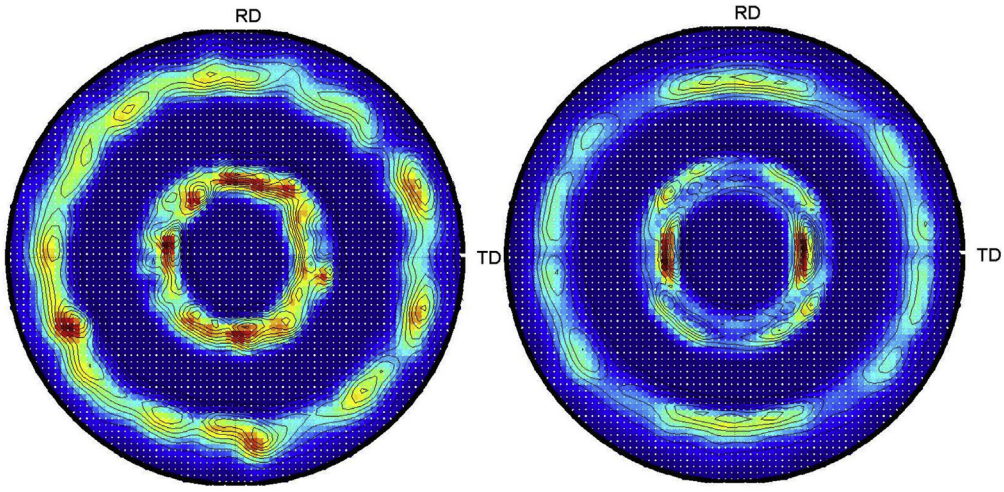

(a) (b)

Fig. 8. {111} Pole figures simulated for equibiaxial tension ($\rho = 1$) at $E_{11} = 0.6$: (a) FC model; (b) SC model.

$$\dot{\boldsymbol{\Sigma}} = \mathbf{L} : \mathbf{G} - \boldsymbol{\Sigma}\,\mathrm{Tr}\,(\mathbf{G}) - \mathbf{G}.\boldsymbol{\Sigma}. \tag{73}$$

Considering that only the components 11, 22, and 33 of the macroscopic velocity gradient **G** are different from zero in the case of tensile states, one can easily conclude that the shearing components of the tangent modulus (L_{1212} for instance) have no influence on the value of $\dot{\Sigma}_{11}$ and, hence, on the evolution of Σ_{11}. This latter result explains why the mechanical (stress–strain) responses are the same for both multiscale schemes, whereas the associated shear tangent moduli are different.

Another observation from Fig. 9 is that, although the component L_{1111} is reduced beyond the elastic range of deformation, it still keeps a very high value (between 1.7×10^5 and 1.8×10^5 MPa) during the subsequent deformation (irrespective of the selected strain path). By contrast, the shearing component L_{1212} is significantly reduced during the deformation and becomes very low (compared to L_{1111}). This observation is a natural outcome of the multi-slip character of crystal plasticity, which leads to the formation of vertices at the current points of the Schmid yield surfaces of single crystals. The reduction of this shearing component is the main destabilizing factor responsible for bifurcation, thus promoting early plastic strain localization (see, e.g., Hutchinson, 1970; Yoshida et al., 2009). A correlation can then be established between the evolution of the shearing components of the tangent modulus, as predicted by both multiscale schemes, and the corresponding limit strains predicted by bifurcation theory. As demonstrated in Fig. 9, the shearing components of the tangent modulus predicted by the self-consistent scheme have a much lower magnitude than their counterparts determined by the Taylor model. As a consequence, the bifurcation-based limit strains predicted by the self-consistent scheme are lower than those predicted by the Taylor model (see Fig. 10 and Fig. 11a). It is worth noting that, when a smooth yield function is used, the shearing component L_{1212} keeps practically the same magnitude as the other components and, consequently, bifurcation is not detected at realistic strain levels. It is also observed from the different curves in Fig. 9 (especially the curves corresponding to the evolution of the shearing component L_{1212}), that the predictions of the FC model are not quite smooth compared to predictions obtained by applying the SC model. This trend is quite expectable, and it is very likely attributable to the fundamental difference in the underlying averaging rules. Indeed, when the Taylor model is used, the different grains deform freely and the interaction between the different grains is obviously neglected. Consequently, the microscopic tangent modulus differs significantly from one grain to another, exhibiting high contrast in its components due to texture evolution. This high contrast results in a rather complex evolution for the components of the macroscopic tangent modulus and, consequently, for the minimal value of the determinant of the polycrystal acoustic tensor over all orientations for the normal to the localization band. This complex evolution leads to the non-smooth curves reported in Fig. 10a. By contrast, when the self-consistent model is used, the interactions between the different grains and their surrounding medium are accounted for. These interactions allow reducing the contrast between the components of the tangent moduli corresponding to the different grains. This reduction in contrast leads to an evolution for the minimal value of the determinant of the polycrystal acoustic tensor that is more regular in the case of the self-consistent scheme than for the Taylor model (see Fig. 10). It should be noted that the same trends have been observed in Franz et al. (2013).

The numerical results obtained by the application of the bifurcation criterion are presented hereafter. This criterion states that strain localization occurs when the minimum of the determinant of the acoustic tensor, over all possible band

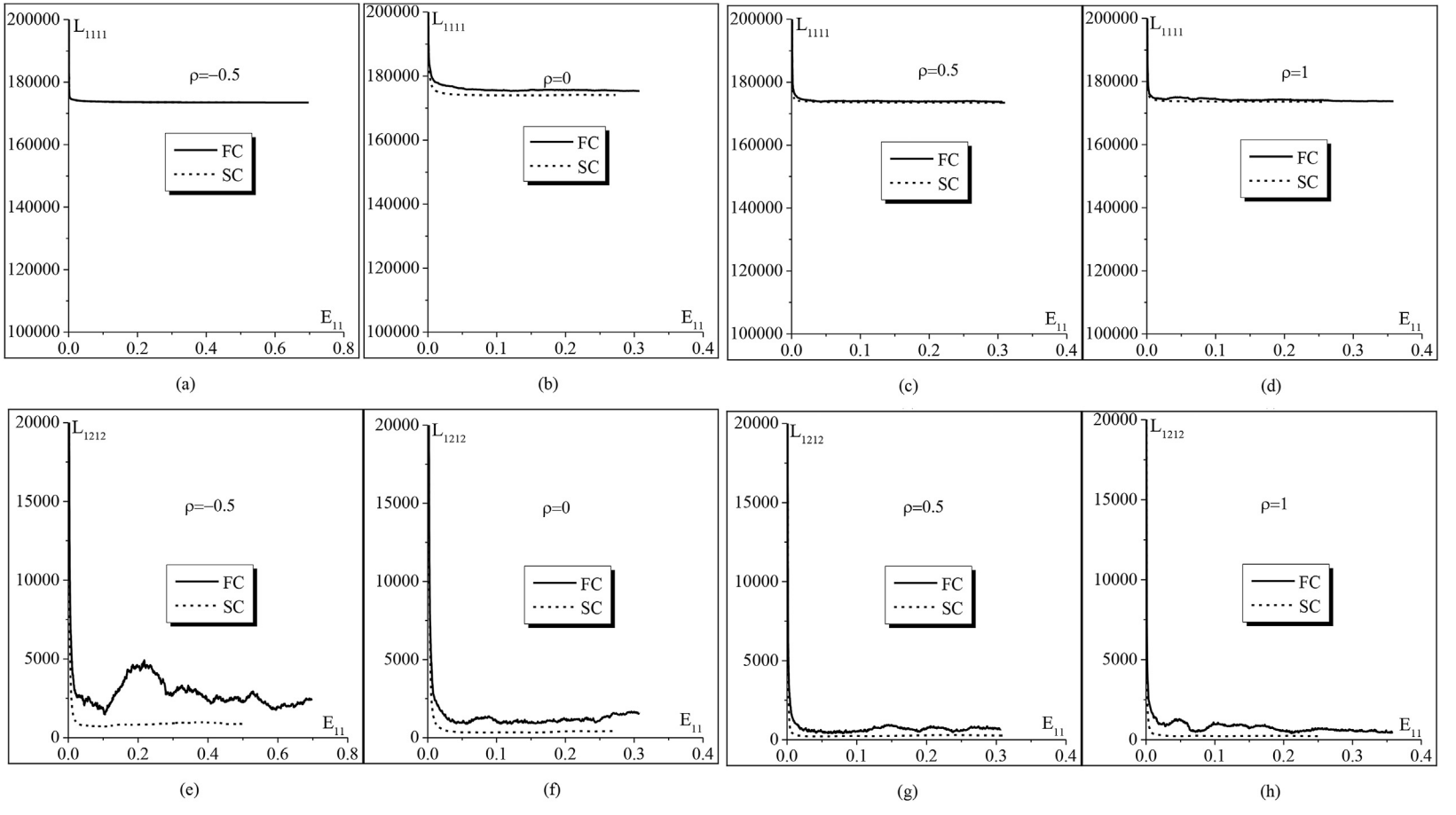

Fig. 9. Evolution of the components L_{1111} and L_{1212} as functions of E_{11}: (a) L_{1111} ($\rho = -0.5$); (b) L_{1111} ($\rho = 0$); (c) L_{1111} ($\rho = 0.5$); (d) L_{1111} ($\rho = 1$); (e) L_{1212} ($\rho = -0.5$); (f) L_{1212} ($\rho = 0$); (g) L_{1212} ($\rho = 0.5$); (h) L_{1212} ($\rho = 1$).

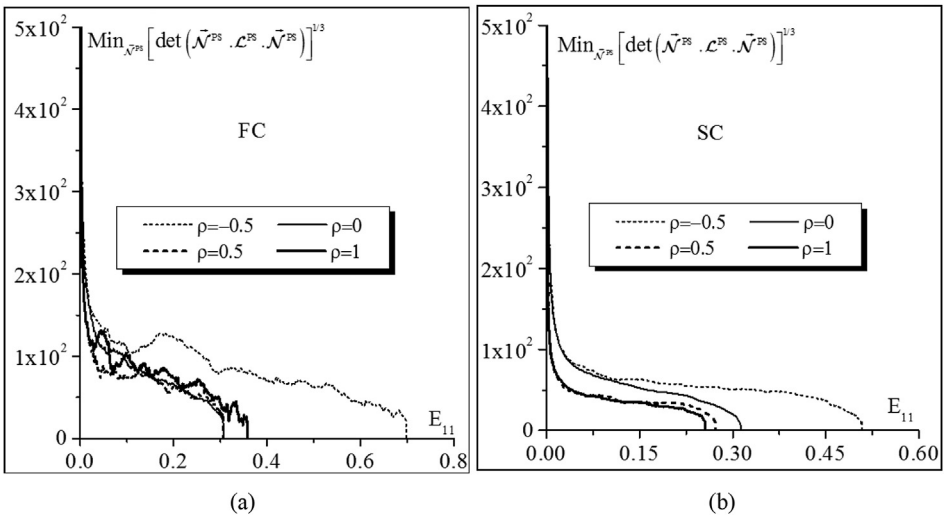

Fig. 10. The minimum of the determinant of the acoustic tensor versus E_{11} for four strain paths ($\rho = -0.5$, $\rho = 0$, $\rho = 0.5$, and $\rho = 1$): (a) FC model; (b) SC model.

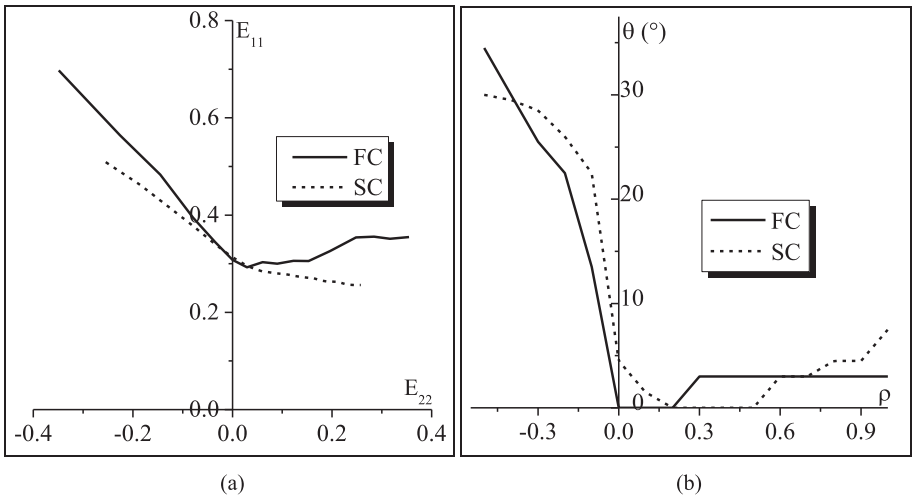

Fig. 11. FLDs and necking band orientations, as predicted by the FC and SC models coupled with bifurcation theory: (a) FLDs; (b) Necking band orientation for the different strain paths.

inclinations, reaches zero. Taking into account the 2D formulation of this criterion, the normal to the band $\overrightarrow{\mathcal{N}}^{PS}$ is restricted to rotate in the sheet plane throughout the straining.

The evolution of the minimum of the determinant of the acoustic tensor, over all possible band inclinations, versus the major strain, is displayed in Fig. 10 for four strain paths ($\rho = -0.5$, $\rho = 0$, $\rho = 0.5$, and $\rho = 1$). As the acoustic tensor is positive definite in the deformation range that precedes the occurrence of localized necking, the unit normal vector $\overrightarrow{\mathcal{N}}^{PS}$, corresponding to the vanishing of its determinant at the onset of localized necking, is the same as that minimizing this determinant. One can observe that, irrespective of the selected strain path and the multi-scale scheme considered, the minimum of that determinant abruptly decreases during the transition between the elastic and plastic regimes, which occurs at small strains. By contrast, in the plastic regime, the decrease is much slower and, accordingly, the minimum of the determinant reaches zero at large strain.

The FLDs predicted by the bifurcation criterion, in conjunction with both the FC and SC models, are shown in Fig. 11a. This figure clearly emphasizes large differences between the FLDs predicted by the two homogenization schemes. Indeed, the limit strains determined with the FC scheme are found to be generally larger than their counterparts predicted by the SC scheme. This observation confirms the recent results of Franz et al. (2013). It can also be seen that the obtained limit strains are monotonically decreasing in the negative ρ range for both scale-transition schemes. However, in the biaxial tension range ($\rho \geq 0$), both the shape and the evolution of the predicted FLDs are more dependent on the adopted homogenization scheme.

Indeed, while the limit strains obtained with the SC multi-scale scheme are still decreasing in the range of positive strain paths, those obtained with the FC model start to increase for strain paths in the range [0.2, 0.7], and eventually exhibit some stagnation for strain paths greater than 0.7. Also, one may notice that the limit strains given by the two averaging schemes are very close in the neighborhood of the plane strain loading path ($\rho = 0$). The larger differences are found near the uniaxial tensile strain path ($\rho = -0.5$), where a maximum gap of 27.5 % may be observed, and the equibiaxial tensile strain path ($\rho = 1$), where a maximum gap of 27.8 % may be recorded. Compared to the results of Yoshida and Kuroda (2012), obtained by coupling the bifurcation criterion with the FC model, the FLD predicted by the BT−FC variant of the present modeling exhibits a similar shape in the negative ρ range. However, in the range of positive strain paths, important differences are observed. As stated in several previous works (see, for instance, Barlat, 1987; Signorelli et al., 2009), the extreme sensitivity of the predicted FLDs to the initial texture in the biaxial tension range ($\rho \geq 0$) seems to be the main reason that could explain these differences.

Fig. 11b shows the necking band inclination θ versus the strain-path ratio ρ, as determined by the two homogenization models. Although, on the whole, the curves describing the localization band orientation follow an evolution that seems to be qualitatively comparable, there are in fact some significant quantitative differences for the necking band orientations predicted by the two averaging schemes. An important observation is that, unlike the vast majority of FLD approaches based on phenomenological constitutive models, the localization band predicted by using crystal plasticity modeling is not necessarily normal to the direction of major strain for the whole range of positive strain paths. This observation is consistent with the results reported in Yoshida and Kuroda (2012).

As suggested by Table 1, one may seek a correlation between the magnitude of the predicted limit strains and the average number of active slip systems (briefly designated hereafter as ANASS). Indeed, Table 1 reveals that, the larger the ANASS, the higher the magnitude of the corresponding limit strain. For instance, when the FC model is applied, it can be seen that the maximum ANASS corresponds to uniaxial tension ($\rho = -0.5$), while the minimum corresponds to plane strain tension ($\rho = 0$). The intermediate values, which are practically identical, correspond to $\rho = 0.5$ and $\rho = 1$. Accordingly, the evolution of the ANASS along the different strain paths matches the evolution of the magnitude of the corresponding limit strains (see Fig. 11a). A similar trend is observed when the SC model is used. Indeed, it can be noticed that the ANASS uniformly decreases when the strain-path ratio increases (in the same way as does the magnitude of the corresponding limit strains in Fig. 11a). It is noteworthy that similar trends were reported earlier in Signorelli et al. (2009), where a viscoplastic self-consistent scheme coupled with the M−K analysis has been used to numerically determine the onset of localized necking for FCC materials.

Table 1
Average Number of Active Slip Systems (ANASS), for four representative strain paths, as determined by each of the two scale-transition schemes.

	$\rho = -0.5$	$\rho = 0$	$\rho = 0.5$	$\rho = 1$
ANASS based on FC model	4.95	4.86	4.94	4.94
ANASS based on SC model	4.92	4.80	4.67	4.55

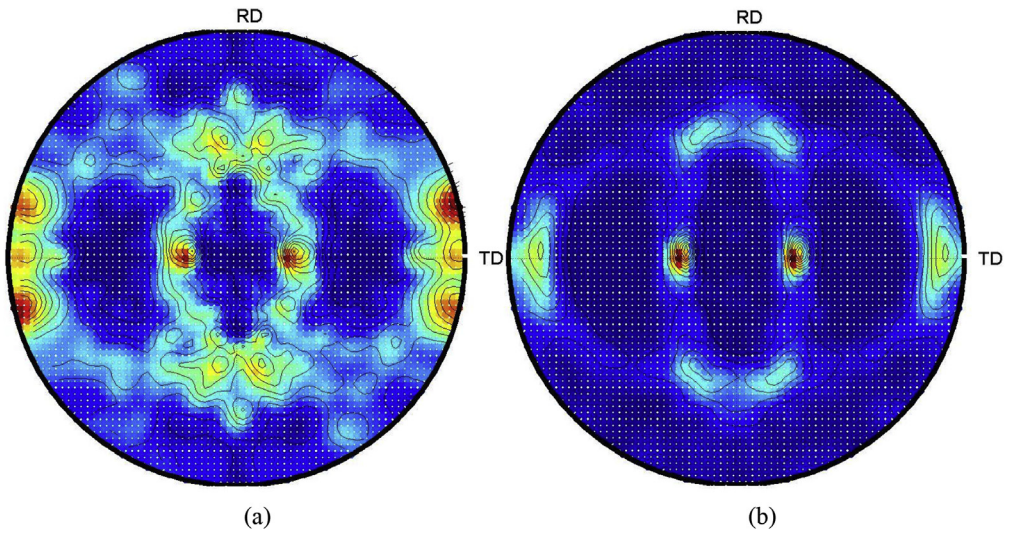

Fig. 12. Final crystallographic textures in terms of {111} pole figures, obtained by coupling the M−K approach with the FC multi-scale scheme, for plane strain tensile state ($\rho = 0$) with a geometric defect ($\xi_I = 5x10^{-3}$) initially normal to the rolling direction: (a) In the safe zone; (b) In the band.

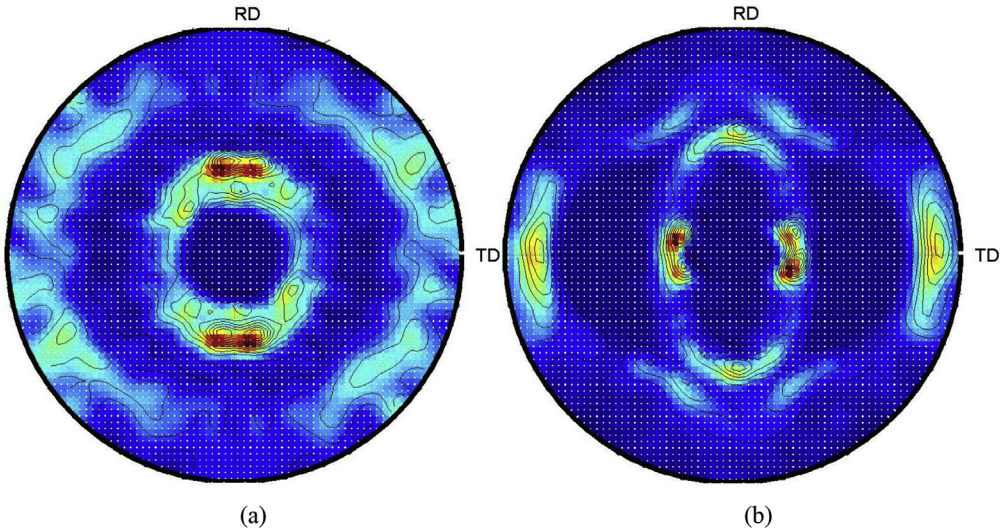

Fig. 13. Final crystallographic textures in terms of {111} pole figures, obtained by coupling the M–K approach with the FC multi-scale scheme, for equibiaxial stretching ($\rho = 1$) with a geometric defect ($\xi_I = 5x10^{-3}$) initially normal to the rolling direction: (a) In the safe zone; (b) In the band.

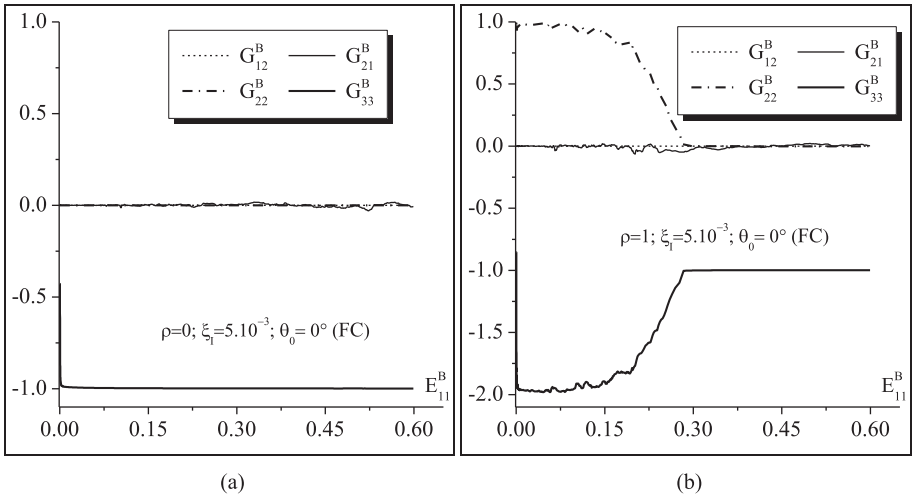

Fig. 14. Normalized components of $\mathbf{G}^B$ as functions of E^B_{11}: (a) Plane strain tension; (b) Equibiaxial tension.

5.3.2. M–K approach

In this section, the M–K approach is used as strain localization criterion. Fig. 12 shows the crystallographic textures predicted by the MK–FC model both in the safe zone and in the band, for a simulated plane strain tensile test ($\rho = 0$). In order to highlight the dissimilarity observed between the two zones, the computations are carried out up to a point well beyond the critical strain ($E^*_{11} = 0.25$), where the components of $\mathbf{G}^B$ are extremely high compared to those of $\mathbf{G}^H$ in the homogeneous zone (which become infinitesimal, as mentioned above). This point corresponds to $E^B_{11} = 0.6$ in the band. In the homogeneous zone, its counterpart keeps practically the same value as the critical strain (due to the magnitude of the components of $\mathbf{G}^H$). Although both textures correspond to a typical plane strain tension texture, they are clearly distinct. Indeed, the texture in the band (see Fig. 12b), which is determined at a higher velocity gradient, is naturally much sharper than that in the homogeneous zone (see Fig. 12a). Similar trends have been observed earlier by Serenelli et al. (2010) within the rigid-viscoplastic framework. In Fig. 13, an analysis similar to the previous one has been performed for equibiaxial tension ($\rho = 1$). It can be noted that, contrary to the components of $\mathbf{G}^H$, which are representative of an equibiaxial tensile state, the components of $\mathbf{G}^B$ tend towards a plane strain tensile state after strain localization. Consequently, the texture in the homogeneous zone appears to be a typical equibiaxial tension texture, whereas its counterpart in the band tends towards a typical plane strain texture. This trend is consistent with a number of literature results, which indicate that irrespective of the boundary conditions imposed to the homogeneous zone, the strain in the band tends towards a typical plane strain state when localization occurs.

The evolution of the components of the velocity gradient $\mathbf{G}^B$ in the band, normalized by the component G^B_{11}, for the two above-mentioned strain paths is illustrated in Fig. 14.

Fig. 15 shows the evolution of the ratio E^B_{11}/E^H_{11}, all along the deformation of the sheet, for different initial imperfection ratios. In this case, a plane strain state ($\rho = 0$) is considered, and the initial band inclination is set to 0° (which corresponds to the actual necking band orientation). The crosses tagged on Fig. 15 indicate the point at which strain localization occurs. The same trends are observed for both FC and SC scale-transition schemes. From Fig. 15a, where the FC model is used, it can be seen that, the lower the initial imperfection ratio, the more abrupt the localization of deformation. Indeed, when the initial imperfection ratio is very small ($\xi_I = 10^{-4}$), the slope of the curve switches instantly from a value very close to zero to a very large value (corresponding to elastic unloading). When the initial imperfection ratio increases, strain localization occurs less abruptly, especially for $\xi_I = 10^{-2}$, where two stages can be distinguished. The first one roughly ranges from $E^H_{11} = 0.05$ to $E^H_{11} = 0.22$, with a very smooth evolution of the ratio E^B_{11}/E^H_{11}. The second stage corresponds to $E^H_{11} > 0.22$. In that stage, the slope increases much more rapidly and eventually becomes very high. The same trend has been observed in Yoshida and Kuroda (2012). Furthermore, it is noteworthy that for relatively large initial imperfection ratios ($\xi_I = 5.\ 10^{-3}$, $\xi_I = 10^{-2}$), at the very early stage of deformation, the equilibrium equation at the interface between the safe zone and the band implies that the magnitudes of the components of the velocity gradient outside the band should be much lower than those inside the band. Consequently, the band undergoes plastic deformation, while the deformation state is still elastic in the homogeneous zone, thus leading to high values for the ratio E^B_{11}/E^H_{11}. This trend can be observed over the range $[0.,\ 5.10^{-2}]$ of E^H_{11}. For subsequent loading, the homogeneous zone also starts undergoing plastic strain, and the ratio decreases and eventually becomes very close to 1. It is worth noting that these trends are in good agreement with the results reported in Yoshida and Kuroda (2012). In Fig. 15b, where the SC averaging scheme is used instead of the FC model, very similar trends are observed as well.

The evolution of the predicted critical strain E^*_{11}, versus the initial band inclination angle θ_0, is displayed in Fig. 16 for four different strain paths. The initial imperfection ratio ξ_I has been taken equal to 10^{-4} in the associated simulations. Two main conclusions can be drawn in view of the obtained numerical results:

- The critical strain E^*_{11} becomes less sensitive to the initial band orientation as the strain path ρ increases. It is also revealed that the curves are continuous, which indicates that 1.5° as increment size is sufficient for pinpointing the band orientation that minimizes the critical strain.
- Some small differences in the trends reflected by the two adopted scale-transition schemes may be emphasized. Indeed, for the SC model (see Fig. 16b), the necking band orientation is equal to 0° for all positive strain paths. However, when the FC model is used, the necking band orientation deviates from 0° for the equibiaxial strain path ($\rho = 1$). Indeed, for this latter strain path, the critical strain E^*_{11} decreases slightly for θ_0 ranging between 0° and 6°, while it slightly increases subsequently. It must be noted that this is in contrast to all phenomenological models studied by the authors, for which the critical strain E^*_{11} is found to be independent of the value of θ_0 for the case of equibiaxial strain path. This point will be further analyzed in what follows (namely, in the discussion relating to Fig. 17).

Fig. 17a compares the FLDs obtained by the application of the initial imperfection approach for the two scale-transition schemes. Recall that, for each value of strain path ($\rho \in [-0.5,\ 1]$), the corresponding limit strain thus predicted represents

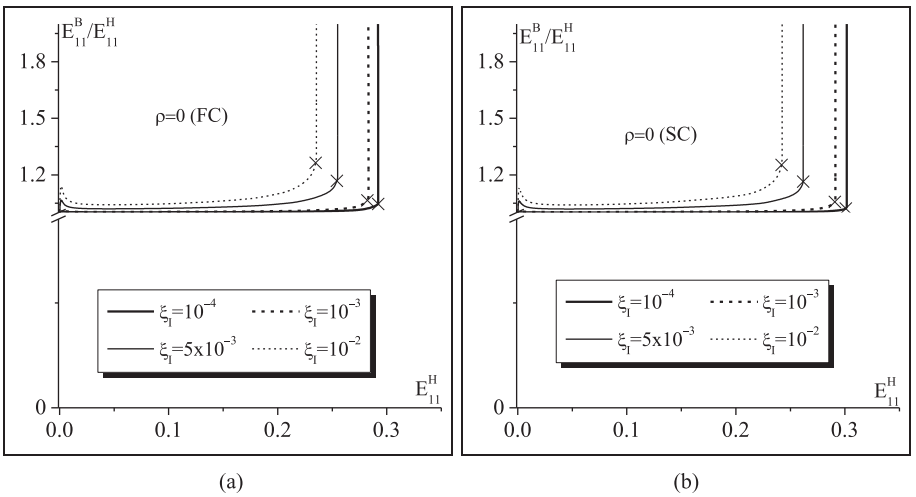

Fig. 15. Normalized component E^B_{11}/E^H_{11} versus the strain component E^H_{11} for plane strain tension ($\rho = 0$) with an imperfection initially oriented at 0° with respect to the major strain direction: (a) FC model; (b) SC model.

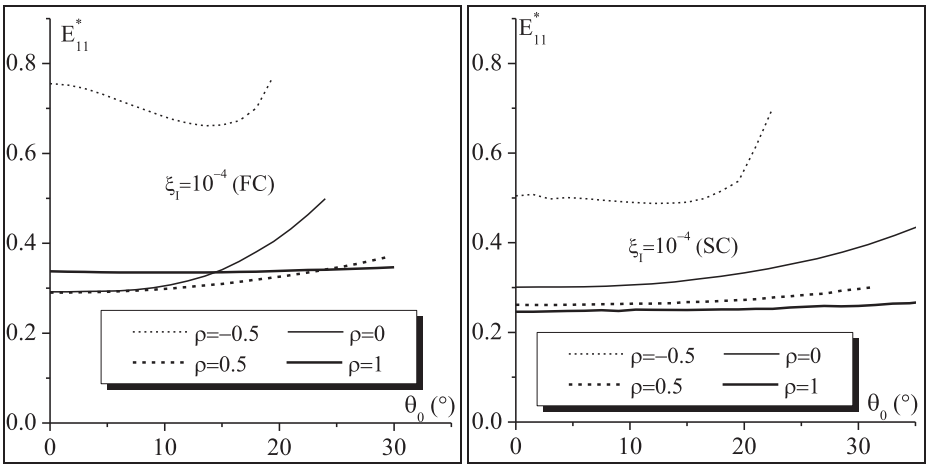

Fig. 16. The critical strain E^{*}_{11} versus the initial band orientation θ_0, for four strain paths ρ and an initial imperfection ratio $\xi_I = 10^{-4}$: (a) FC model; (b) SC model.

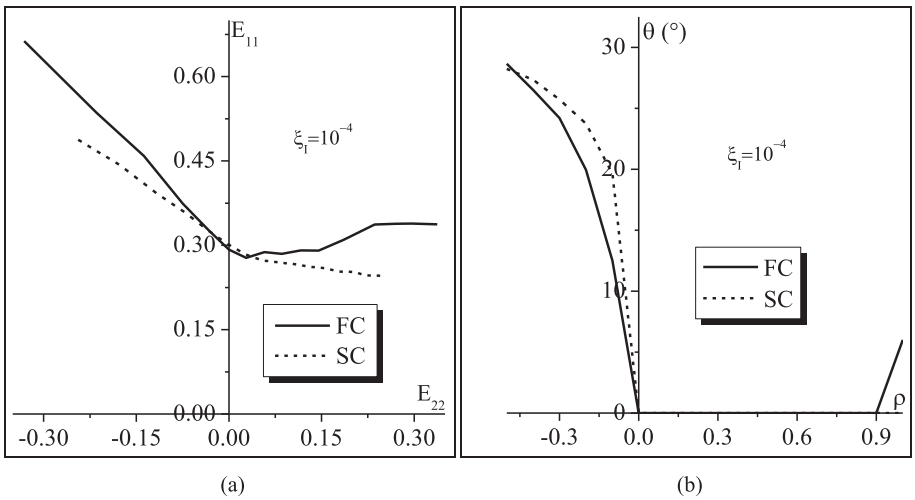

Fig. 17. FLDs and necking band orientations, as predicted by the FC and SC models coupled with the M−K analysis, for an initial imperfection ratio $\xi_I = 10^{-4}$: (a) Predicted FLDs; (b) Necking band orientation versus ρ.

the minimum of the critical strains over all possible band orientations ($\theta_0 \in [0^\circ,\ 90^\circ]$). Here, the initial imperfection ratio ξ_I is taken equal to 10^{-4}. The trend obtained with the M−K analysis (see Fig. 17a) is the same as that given by the bifurcation theory (see Fig. 11a): the SC scheme tends to predict lower forming limits than the FC model. The results displayed in Figs. 11a and 17a clearly illustrate the differences between the FC and SC multiscale schemes, particularly in the biaxial stretching range, although the shapes and levels of the FLDs are more similar in the negative minor-strain range. The difference between the FLDs predicted by both homogenization approaches may be explained by the difference in the crystallographic texture evolution, which is well known to be an important factor that strongly affects the FLDs, especially in the vicinity of equibiaxial stretching (Barlat, 1987). Indeed, using the same initial crystallographic texture with the two multiscale schemes, one can obtain different final crystallographic textures. This variance is due to the difference in the modeling of the local deformation, as described by the two homogenization schemes. Furthermore, formability may be influenced by other microstructural parameters, such as the grain shape. In fact, contrary to the FC model, the SC model has the capability of taking the grain shape and its evolution into account during the deformation. To our best knowledge, this is the first time the forming limit diagrams predicted by the FC model are compared to those predicted by the SC model within a rate-independent single crystal plasticity framework. However, there exist in the literature some comparisons between the limit strains predicted by both multiscale schemes within the framework of rate-dependent crystal plasticity. In this field, one can quote Singorelli et al., (2012), who have demonstrated that the SC model tends to give lower forming limits than the FC model. However, the same authors have obtained opposite trends in (Signorelli et al., 2009; Serenelli et al., 2011) for rate-dependent materials: the

SC multiscale model has been shown to give a higher FLD than the FC model. The difference in the trends reported in Signorelli et al. (2009) and Serenelli et al. (2011) and those given by our current numerical results could be explained by the difference between the adopted initial textures and the corresponding evolutions during the deformation. In fact, the texture evolution is directly related to the evolution of the slip rates of the different crystallographic slip systems. Within a rate-dependent formulation, there is no decomposition of the slip systems into "active" or "inactive" sets; instead, all slip systems are active along the deformation, and the difference between slip systems is governed by the corresponding slip rate, which depends on the current resolved and critical shear stresses. By contrast, within a rate-independent formulation, the slip rates of the different slip systems are determined by the numerical algorithm given in Section 2.2. Consequently, both formulations (rate-dependent and rate-independent) provide different predictions in terms of slip rates and, accordingly, in terms of texture evolution. In contrast to the trends presented in the current paper or in (Signorelli et al., 2009; Serenelli et al., 2011; Signorelli et al., 2012), Tadano et al. (2013) have shown that the FC and the CPFEM models lead to almost the same forming limit diagrams. This result may be explained by the effect on texture evolution of the adopted multiscale scheme. Indeed, in the current paper as well as in (Signorelli et al., 2009; Serenelli et al., 2011; Signorelli et al., 2012), it is the self-consistent approach that has been used to derive the mechanical behavior of the polycrystalline aggregate from the mechanical behavior of the microscopic constituents. However, in Tadano et al. (2013), it is the CPFEM method that has been used instead.

The necking band orientation θ, which corresponds to the onset of localized necking, is shown in Fig. 17b for the full range of strain paths ρ. It can be observed that, on the whole, the predicted band orientations are similar to those obtained with the bifurcation approach. However, in the present case of M−K analysis, the differences between the FC and SC models are less pronounced in the biaxial tension range ($\rho > 0$). Indeed, whatever the model used, FC or SC, the predictions show that the necking band remains normal to the rolling direction when the value of ρ is comprised between 0 and 0.9. For the equibiaxial tensile state ($\rho = 1$), however, the normal to the band departs slightly from the direction of rolling (with an inclination of 5°) when the FC model is used, while it remains along the rolling direction for the SC model.

5.3.3. Comparison between bifurcation theory and initial imperfection approach

The impact of the initial imperfection ratio ξ_I on the predicted critical strains E^*_{11} is depicted in Fig. 18. In this figure, the evolution of E^*_{11} versus the initial band inclination angle θ_0 is shown for different values of initial imperfection ratio ξ_I in the case of plane strain tensile state. For all initial band orientations, it is clearly shown that E^*_{11} decreases monotonically as the initial imperfection ratio ξ_I increases, irrespective of the scale-transition scheme used. It can also be seen that the necking band orientation predicted in plane strain tension is equal to 0°, for both multi-scale models and all initial imperfection ratios. In addition, E^*_{11} tends to a threshold value when the ratio ξ_I tends to zero. From the theoretical formulations developed in Section 4.1.3, it is expected that this threshold value is the limit strain predicted by bifurcation theory. This important issue is discussed in depth hereafter (see Fig. 20, where the FLDs predicted by bifurcation theory are compared to those predicted by M−K analysis).

As demonstrated in Fig. 18, an increase in the amount of initial imperfection results in a decrease in the limit strains. To further illustrate this feature, Fig. 19 shows the evolution of the limit strain E_{11} versus the initial imperfection size ξ_I for four strain paths ρ. Note that, in this figure, the limit strain corresponding to the abscissa $\xi_I = 0$ is the one predicted by the bifurcation criterion. It can be clearly observed that the limit strain decreases when the initial imperfection increases, for all

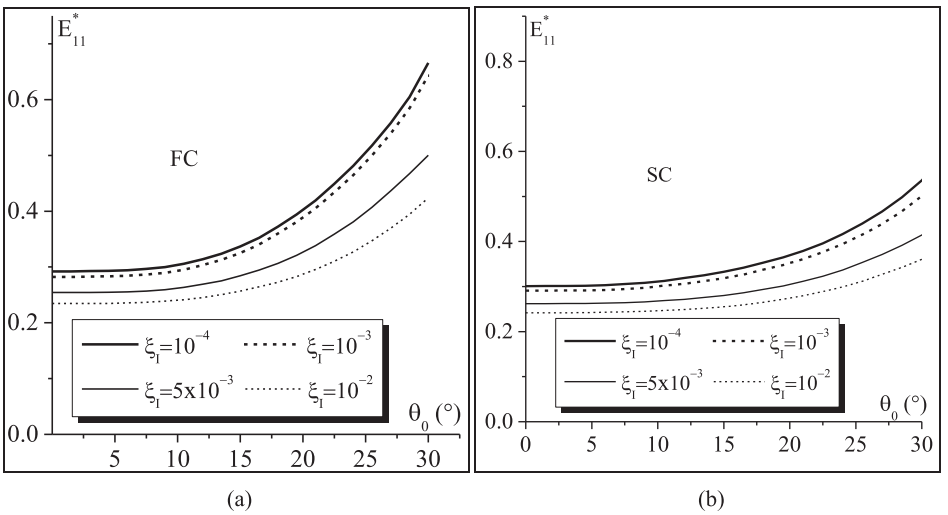

Fig. 18. The critical strain E^*_{11} versus the initial band inclination θ_0, for plane strain tension ($\rho = 0$) and different initial imperfection ratios: (a) FC model; (b) SC model.

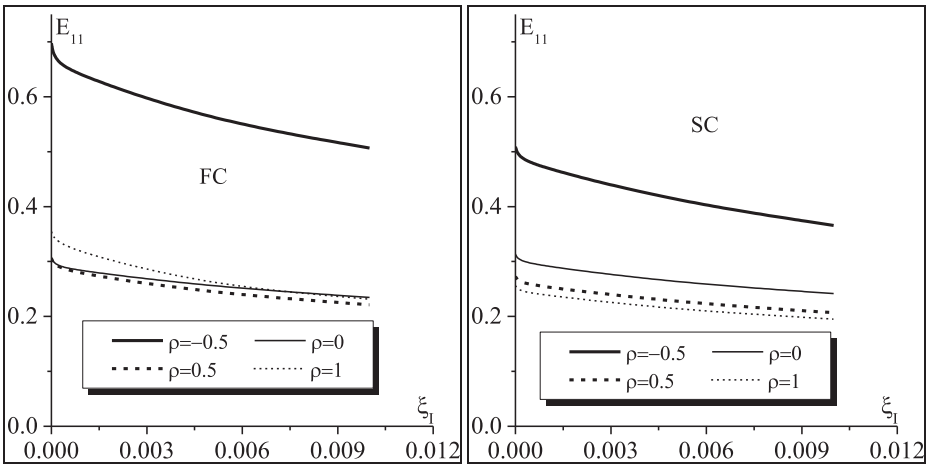

Fig. 19. The limit strain E_{11} versus the initial imperfection ratio ξ_I, for four strain paths ρ: (a) FC model; (b) SC model.

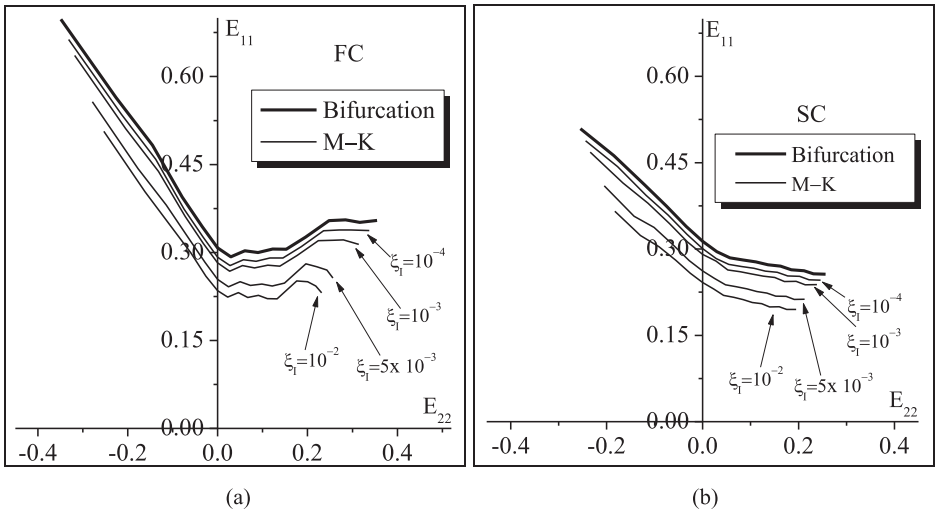

Fig. 20. Comparison between the FLDs predicted by M–K analysis ($\xi_I = 10^{-4}$; $\xi_I = 10^{-3}$; $\xi_I = 5x10^{-3}$; $\xi_I = 10^{-2}$) and the FLD predicted by bifurcation theory: (a) FC model; (b) SC model.

strain paths ρ investigated. Moreover, this result is valid for both multi-scale models. This dependence of the predicted limit strains on the amount of initial imperfection was previously studied using multi-scale rate-dependent approaches (Zhou and Neale, 1995; Signorelli et al., 2009) as well as rate-independent crystal plasticity modeling (Yoshida and Kuroda, 2012). The results found in the current contribution are consistent with those reported in the above investigations.

The comparison between the FLDs predicted by bifurcation theory and those determined by M–K analysis is shown in Fig. 20. Four different initial imperfection ratios are considered: $\xi_I = 10^{-4}$, $\xi_I = 10^{-3}$, $\xi_I = 5x10^{-3}$, and $\xi_I = 10^{-2}$. It is found that the FLD predicted by bifurcation theory represents an upper limit to those obtained with the initial imperfection model. Moreover, this result is valid for both scale-transition schemes, namely the FC and SC models. Indeed, Fig. 20 demonstrates that the limit strains computed by the M–K approach tend towards those determined by bifurcation theory when the size of initial imperfection ξ_I tends towards zero. In short, the impact of initial imperfection mainly consists in shifting the FLD downwards. Considering the similarity in the mathematical formulations of the two localization criteria, this trend is quite expectable: the initial imperfection approach reduces to the bifurcation analysis if the amount of initial imperfection is set to zero. The FLDs shown in Fig. 20 also confirm that the trend preliminarily emphasized in Figs. 18 and 19, in the case of plane strain loading, is more generally valid for the whole ρ range. This result has already been shown within phenomenological constitutive frameworks (see, for instance, Ben Bettaieb and Abed-Meraim, 2015). However, this has been much less frequently investigated with multi-scale modeling approaches. In the latter context, a recent investigation has been carried

out by Yoshida and Kuroda (2012). In this latter contribution, only the FC model was used as scale-transition scheme. Yoshida and Kuroda (2012) have shown that the limit strains increase with decreasing the amount of initial imperfection, and tend to saturate beneath the values of the limit strains predicted by bifurcation theory, except for strain ratios near equibiaxial stretching. Around the equibiaxial stretching mode, Yoshida and Kuroda (2012) found that the limit strains increase as the initial imperfection decreases and exceed the limit strains given by bifurcation theory for $\xi_I = 10^{-4}$. The difference in the trends obtained with the Taylor model, in the two contributions (Yoshida and Kuroda, 2012 and the current work), is likely to originate from the difference in the initial crystallographic textures used as "input" for the different simulations. Indeed, the limit strains predicted by both the bifurcation analysis and the initial imperfection approach, particularly around the equibiaxial stretching mode, are very sensitive to slight differences in crystallographic texture. The extreme influence of deformation-induced textures and anisotropy on the localization of plastic flow has been earlier highlighted in several pioneering works, such as Asaro and Needleman (1985) and Barlat (1987).

In Fig. 21, the above comparisons between the bifurcation approach and the M–K analysis, in terms of their respective predictions of limit strains, are further completed in terms of necking band orientations. From that figure, the following observations can be made:

- When the M–K analysis is applied, the necking band inclination angle is equal to zero for almost all strain paths in the biaxial tension range ($\rho > 0$).
- In the negative ρ range, the value of necking band inclination angle decreases when the value of ρ increases. For a given strain path ρ, the necking band inclination angle also decreases when the size of initial imperfection increases.
- On the whole, the two multi-scale models reveal the same trends for the evolution of the necking band orientation, although this localization band orientation appears to be more sensitive to the initial imperfection size when the SC model is used.

5.4. *Sensitivity of the predicted FLDs to the initial crystallographic texture*

It is widely recognized that the initial crystallographic texture strongly affects both the shape and the overall level of the predicted FLDs (Yoshida and Kuroda, 2012; Bertinetti et al., 2014). In order to assess this aspect with the proposed modeling framework, two different initial crystallographic textures for the polycrystalline aggregate are considered in addition to the previous one (as described in Fig. 5). In what follows, the texture introduced in Fig. 5 and the two new textures will be referred to as Texture I, Texture II and Texture III, respectively. Textures II and III are obtained from Texture I by replacing 500, respectively, 1000 of its constituent grains by other grains of arbitrary orientations. Fig. 22a and b show the {111} pole figures associated with Texture II and Texture III, respectively. It can be seen that these textures are not very different from the initial texture (Texture I).

The effect of the initial crystallographic texture both on the location and on the shape of the FLDs predicted by the different localization approaches and averaging models is depicted in Fig. 23. On the whole, it can be seen that the sensitivity of the predicted limit strains to the initial texture remains quite low in the range of negative strain paths. However, in the range of positive strain paths, the opposite trend is observed. Indeed, both the shape and the overall level of the predicted FLDs are very sensitive to the initial texture. This observation is consistent with previous pioneering works, such as Barlat (1987).

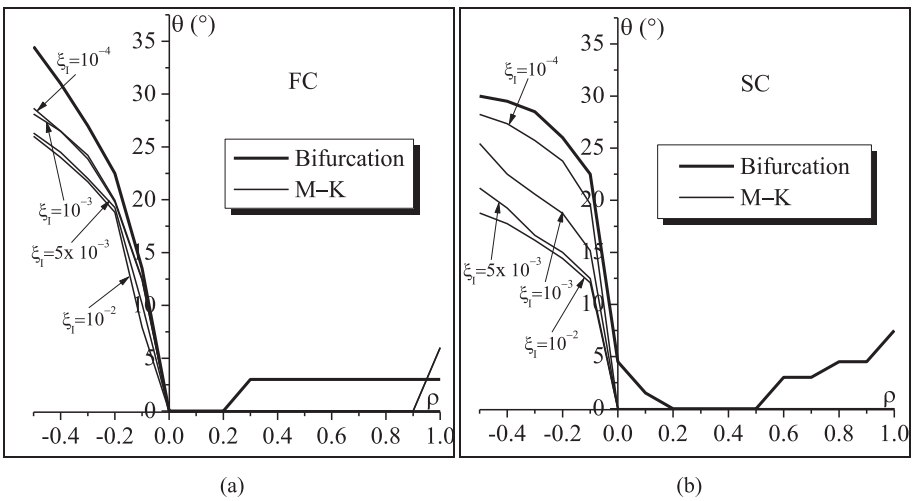

Fig. 21. Comparison between the necking band inclinations given by the M–K analysis ($\xi_I = 10^{-4}$; $\xi_I = 10^{-3}$; $\xi_I = 5x10^{-3}$; $\xi_I = 10^{-2}$) and those yielded by the bifurcation criterion: (a) FC model; (b) SC model.

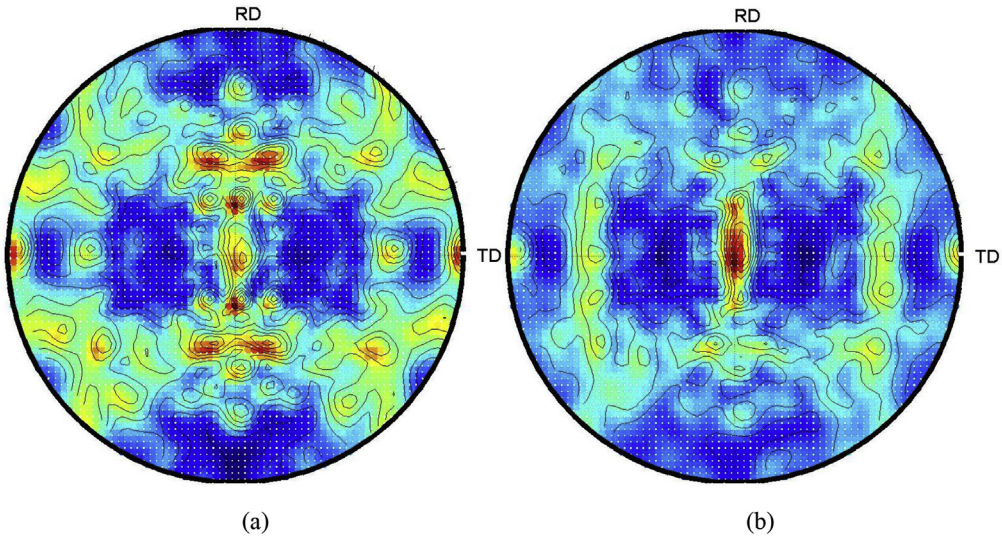

Fig. 22. {111} Pole figures for: (a) Texture II; (b) Texture III.

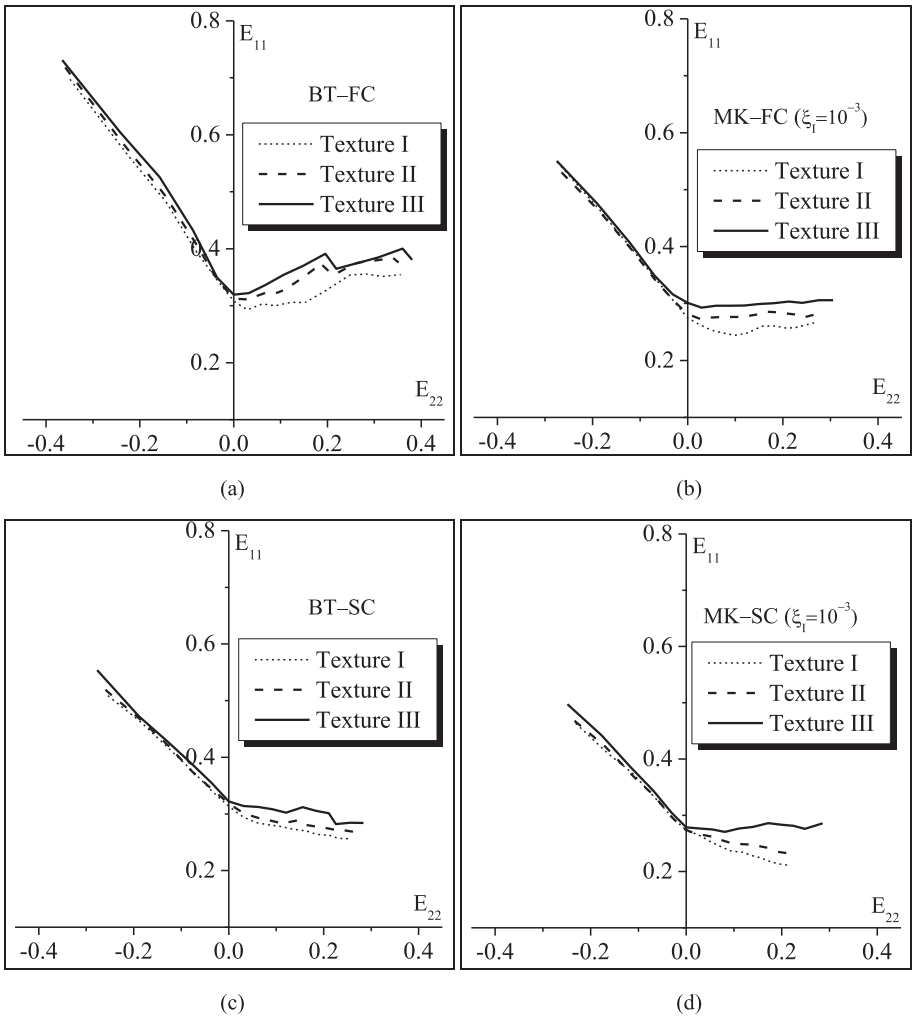

Fig. 23. Effect of the initial crystallographic texture on the predicted FLDs: (a) BT–FC model; (b) MK–FC model ($\xi_I = 10^{-3}$); (c) BT–SC model; (d) MK–SC model ($\xi_I = 10^{-3}$).

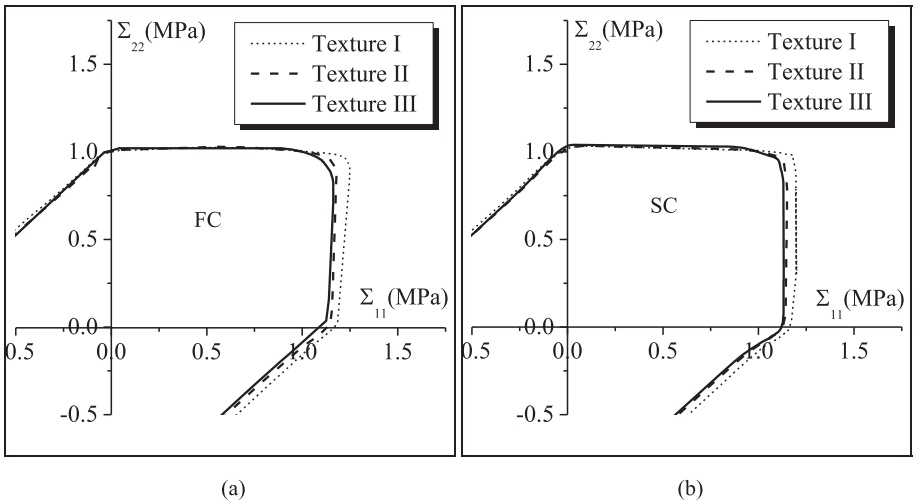

Fig. 24. Yield surfaces for the three different crystallographic textures investigated at equibiaxial strain localization: (a) FC model; (b) SC model.

Furthermore, for positive strain paths, the gaps between the predicted FLDs are more pronounced with the M−K analysis (see Fig. 23b and d), as compared to bifurcation theory (see Fig. 23a and c). Besides, Fig. 23a reveals that the FLDs predicted by bifurcation theory coupled with the FC model exhibit a fall near equibiaxial tension ($\rho = 1$) for Textures II and III, in contrast to the case of Texture I. In Fig. 23c, the same localization criterion (bifurcation theory) coupled with the SC model leads to the formation of a plateau in the neighborhood of equibiaxial tension for Texture III. All these results illustrate the strong and complex influence of the initial texture on the predicted FLDs.

It is well known that, for loading paths close to equibiaxial tension, the values of the predicted limit strains for a material are closely related to the sharpness of the associated yield surface (see, e.g., Neale and Chater, 1980; Lian et al., 1989; Kuroda and Tvergaard, 2000; Signorelli et al., 2012). To further assess this correlation, we plot in Fig. 24 the yield surfaces corresponding to the three above-described textures at equibiaxial strain localization, as predicted by the FC and SC models (see Fig. 24a and b, respectively). Similar to some studies in the literature (see, e.g., Wu et al., 2004), these yield surfaces are normalized by their corresponding equibiaxial yield stresses ($\Sigma_{11} = \Sigma_{22}$), in order to underline their differences in terms of sharpness. In accordance with several literature results, a correlation between the overall level of the FLDs, in the neighborhood of equibiaxial tension, and the degree of sharpness of the associated yield surfaces may be clearly established. The sharper the yield surface, the lower the corresponding FLD.

6. Concluding remarks

In this paper, an efficient numerical tool has been developed, which is specifically designed to the prediction of forming limit diagrams for elasto-plastic sheet metals undergoing proportional strain paths. This tool is based on strong coupling between a micromechanical model and two localization criteria. For the micromechanical modeling, an implicit iterative scheme, belonging to the category of ultimate algorithms, has been developed to integrate the single crystal constitutive equations. This implicit scheme allows considering relatively large time increments and, consequently, significantly reduces the computational time. At the polycrystalline scale, a theoretical framework has been presented for the incremental self-consistent multi-scale scheme, which is then utilized to compute the overall tangent modulus linking the velocity gradient of the polycrystal to its nominal stress rate. The algorithmic aspects concerning the implementation of this multi-scale model have also been provided. For predicting the limit strains of the polycrystalline aggregate, two localization criteria, namely the bifurcation approach and the M−K analysis, have been revisited with a formulation that is well-adapted to the polycrystal constitutive relations. Relevant aspects of the numerical implementation have been discussed for both localized necking criteria, and particular attention has been devoted to the efficient and accurate resolution of the non-linear equations governing the M−K analysis.

Using the theoretical and numerical tools developed above, various numerical investigations have been conducted in order to predict the limit strains and associated FLDs for polycrystalline materials. From all of these simulation results, which allowed multiple cross comparisons, it appears that the selected scale-transition scheme greatly influences both the overall level and the shape of the predicted FLDs. On the other hand, extensive comparisons between the two localization criteria demonstrate that the FLD computed by bifurcation theory represents an upper limit to those predicted by M−K analysis. It is also demonstrated that when the initial imperfection ratio involved in the initial imperfection analysis tends towards zero, the associated FLDs tend towards the bifurcation-based FLD. It is noteworthy that these important results, which have already

been discussed for phenomenological constitutive models, are shown here to be valid for both scale-transition schemes, namely the FC and SC models.

Appendix A. Main lines of the Newton–Raphson method used to solve the self-consistent equations

To solve the self-consistent equations and then to compute the macroscopic tangent modulus, the Newton–Raphson method is used when the fixed point method detailed in Section 3.2 fails to converge. To apply this Newton–Raphson method over a typical time increment, we assume that the microscopic tangent modulus $\mathbf{l}^{I}$, the volume fraction f^{I} and the interaction tensors T^{II}, for each grain I that composes the polycrystalline aggregate, do not change from one iteration to another. This assumption has a negligible effect on the accuracy of the numerical results and the stability of the general numerical scheme. Let us recall the main equations to be solved by applying this Newton–Raphson method:

$$\mathbf{A}^{I} = \left(\mathbf{I}_4 - \mathbf{T}^{II}\colon(\mathbf{l}^{I} - \mathbf{L})\right)^{-1} \colon \langle \left(\mathbf{I}_4 - \mathbf{T}^{II}\colon(\mathbf{l}^{I} - \mathbf{L})\right)^{-1} \rangle^{-1} \quad ; \quad I = 1, \ldots, N_g. \tag{A.1}$$

$$\mathbf{L} = f^{I}\ \mathbf{l}^{I}\colon \mathbf{A}^{I} \text{ (with summation over I)}. \tag{A.2}$$

Eqs. (A.1) and (A.2) correspond in fact to Eqs. (43) and (45), respectively. Taking into consideration the above assumption, we can easily deduce that the unique unknown of the self-consistent problem, summarized by Eq. (A.1) and (A.2), is the macroscopic tangent modulus $\mathbf{L}$. The equation to be solved to compute $\mathbf{L}$ is the following:

$$\mathscr{R} = \mathbf{L} - f^{I}\ \mathbf{l}^{I}\colon \mathbf{A}^{I} = \mathbf{0}, \tag{A.3}$$

where 0 is the fourth-order zero tensor. To solve Eq. (A.3), the Newton–Raphson method is used. The standard update relation for the macroscopic tangent modulus at iteration (s) results in:

$$\mathbf{L}^{(s+1)} = \mathbf{L}^{(s)} + d\mathbf{L}^{(s)}, \tag{A.4}$$

where

$$d\mathbf{L}^{(s)} = -\mathscr{D}^{(s)^{-1}} \mathscr{R}^{(s)}. \tag{A.5}$$

Here, $\mathscr{D}^{(s)}$ is the sth iteration of the Jacobian matrix defined as $(\partial\mathscr{R}/\partial\mathbf{L})$. The components of this Jacobian matrix could be determined by using Eq. (A.1) and (A.3). As well-known from several other classical numerical problems, and confirmed by the numerical developments carried out in the current paper, the use of the Newton–Raphson algorithm ensures quasi-permanent convergence but requires a CPU time larger than that required when the fixed point method is applied. This increase in the CPU time is due to the computation and the inversion of the Jacobian matrix $\mathscr{D}$. For this reason, we decided to systematically apply the fixed point method to compute the macroscopic tangent modulus, and to use the Newton–Raphson procedure only as alternative in case the former method fails to converge.

References

Abed-Meraim, F., Balan, T., Altmeyer, G., 2014. Investigation and comparative analysis of plastic instability criteria: application to forming limit diagrams. Int. J. Adv. Manuf. Technol. 71 (5–8), 1247–1262.

Ahzi, S., Molinari, A., Canova, G.R., 1990. Effect of the grain shape on the texture evolution of a polycrystalline material. In: Boehler, J.P. (Ed.), Yielding, Damage and Failure of Anisotropic Solids, EGF5. Mechanical Engineering Publ., London, pp. 425–441.

Akpama, H.K., Ben Bettaieb, M., Abed-Meraim, F., 2016. Numerical integration of rate-independent BCC single crystal plasticity models: comparative study of two classes of numerical algorithms. Int. J. Num. Meth. Eng. 108, 363–422.

Allwood, J.M., Shouler, D.R., 2009. Generalised forming limit diagrams showing increased forming limits with non-planar stress states. Int. J. Plast. 25, 1207–1230.

Anand, L., Kothari, M., 1996. A computational procedure for rate-independent crystal plasticity. J. Mech. Phys. Solids 44 (4), 525–558.

Asaro, R.J., Needleman, A., 1985. Texture development and strain hardening in rate dependent polycrystals. Acta Metall. 33, 923–953.

Barlat, F., 1987. Crystallographic texture, anisotropic yield surfaces and forming limits of sheet metals. Mat. Sci. Eng. 91, 55–72.

Ben Bettaieb, M., Abed-Meraim, F., 2015. Investigation of localized necking in substrate-supported metal layers: comparison of bifurcation and imperfection analyses. Int. J. Plast. 65, 168–190.

Ben Bettaieb, M., Débordes, O., Dogui, A., Duchêne, L., Keller, C., 2012. On the numerical integration of rate independent single crystal behavior at large strain. Int. J. Plast. 32–33, 184–217.

Bertinetti, M.A., Schwindt, C.D., Signorelli, J.W., 2014. Effect of the cube orientation on formability for FCC materials: a detailed comparison between full-constraint and self-consistent predictions. Int. J. Mech. Sci. 87, 200–217.

Berveiller, M., Fassi-Fehri, O., Hihi, A., 1987. The problem of two plastic and heterogeneous inclusions in an anisotropic medium. Int. J. Eng. Sci. 25 (6), 691–709.

Bishop, J.F.W., Hill, R., 1951. A theory of the plastic distortion of a polycrystalline aggregate under combined stresses. Phil. Mag. 42, 414–427.

Borja, R.I., Wren, J.R., 1993. Discrete micromechanics of elastoplastic crystals. Int. J. Numer. Methods Eng. 36, 3815–3840.

Chung, K., Kim, H., Lee, C., 2014. Forming limit criterion for ductile anisotropic sheets as a material property and its deformation path insensitivity. Part I: deformation path insensitive formula based on theoretical models. Int. J. Plast. 58, 3–34.

Dillamore, I.L., Katoh, H., 1974. The mechanisms of recrystallization in cubic metals with particular reference to their orientation-dependence. J. Metal. Sci. 8, 73–83.

Eyckens, P., Van Bael, A., Van Houtte, P., 2011. An extended Marciniak–Kuczynski model for anisotropic sheet subjected to monotonic strain paths with through-thickness shear. Int. J. Plast. 27, 1577–1597.
Fischer, A., 1992. A special Newton-type optimization method. Optimization 24, 269–284.
Fischer, A., 1997. Solution of monotone complementarity problems with locally Lipschitzian functions. Mathematical Programming 76, 513–532.
Franz, G., Abed-Meraim, F., Lorrain, J.P., Ben Zineb, T., Lemoine, X., Berveiller, M., 2009a. Ellipticity loss analysis for tangent moduli deduced from a large strain elastic–plastic self-consistent model. Int. J. Plast. 25, 205–238.
Franz, G., Abed-Meraim, F., Ben Zineb, T., Lemoine, X., Berveiller, M., 2009b. Strain localization analysis using a multiscale model. Comput. Mat. Sci. 45, 768–773.
Franz, G., Abed-Meraim, F., Berveiller, M., 2013. Strain localization analysis for single crystals and polycrystals: towards microstructure-ductility linkage. Int. J. Plast. 48, 1–33.
Haddag, B., Abed-Meraim, F., Balan, T., 2009. Strain localization analysis using a large deformation anisotropic elastic–plastic model coupled with damage. Int. J. Plast. 25, 1970–1996.
Harren, S.V., Asaro, R.J., 1989. Nonuniform deformations in polycrystals and aspects of the validity of the Taylor model. J. Mech. Phys. Solids 37, 191–232.
Harren, S.V., Lowe, T.C., Asaro, R.J., Needleman, A., 1989. Analysis of large-strain shear in rate-dependent face-centred cubic polycrystals: correlation of micro- and macromechanics. Phil. Trans. R. Soc. A 328, 443–500.
Harren, S.V., 1991. The finite deformation of rate-dependent polycrystals–II: a comparison of the self-consistent and Taylor methods. J. Mech. Phys. Solids 39 (3), 361–383.
Hill, R., 1952. On discontinuous plastic states, with special reference to localized necking in thin sheets. J. Mech. Phys. Solids 1, 19–30.
Hutchinson, J.W., 1970. Elastic plastic behaviour of polycrystalline metals and composites. Proc. R. Soc. Lond. A 319, 247–272.
Jeong, Y., Pham, M.-S., Iadicola, M., Creuziger, A., Foecke, T., 2016. Forming limit prediction using a self-consistent crystal plasticity framework: a case study for body-centered cubic materials. Model. Simul. Mat. Sci. Eng. 24 (5), 055005.
Keeler, S.P., Backofen, W.A., 1963. Plastic instability and fracture in sheets stretched over rigid punches. Trans. ASM 56, 25–48.
Khan, A.S., Baig, M., 2011. Anisotropic responses, constitutive modeling and the effects of strain-rate and temperature on the formability of an aluminum alloy. Int. J. Plast. 27, 522–538.
Knockaert, R., Chastel, Y., Massoni, E., 2002. Forming limits predictions using rate-independent polycrystalline plasticity. Int. J. Plast. 18, 231–247.
Kuroda, M., Tvergaard, V., 2000. Forming limit diagrams for anisotropic metal sheets with different yield criteria. Int. J. Solids. Struct. 37 (37), 5037–5059.
Lebensohn, R.A., Tomé, C.N., 1994. A self-consistent viscoplastic model: prediction of rolling textures of anisotropic polycrystals. Mat. Sci. Eng. A 195, 71–82.
Lévesque, L., Inal, K., Neale, K.W., Mishra, R.K., 2010. Numerical modeling of formability of extruded magnesium alloy tubes. Int. J. Plast. 26, 65–83.
Li, J., Carsley, J.E., Stoughton, T.B., Hector Jr., L.G., Hu, S.J., 2013. Forming limit analysis for two-stage forming of 5182-O aluminum sheet with intermediate annealing. Int. J. Plast. 45, 21–43.
Lian, J., Barlat, F., Baudelet, B., 1989. Plastic behavior and stretchability of sheets metals. Part II: effect of yield surface shape on sheet forming limit. Int. J. Plast. 5, 131–147.
Lipinski, P., Berveiller, M., 1989. Elastoplasticity of micro-inhomogeneous metals at large strains. Int. J. Plast. 5, 149–172.
Manopulo, N., Hora, P., Peters, P., Gorji, M., Barlat, F., 2015. An extended modified maximum force criterion for the prediction of localized necking under non-proportional loading. Int. J. Plast. 75, 189–203.
Mansouri, L.Z., Chalal, H., Abed-Meraim, F., 2014. Ductility limit prediction using a GTN damage model coupled with localization bifurcation analysis. Mech. Mater 76, 64–92.
Marciniak, Z., Kuczynski, K., 1967. Limit strains in processes of stretch-forming sheet metal. Int. J. Mech. Sci. 9 (9), 609–620.
Miehe, C., Schröder, J., 2001. A comparative study of stress update algorithms for rate-independent and rate-dependent crystal plasticity. Int. J. Num. Meth. Eng. 50, 273–298.
Neale, K.W., Chater, E., 1980. Limit strain predictions for strain-rate sensitive anisotropic sheets. Int. J. Mech. Sci. 22, 563–574.
Nebozhyn, M.V., Gilormini, P., Ponte Castañeda, P., 2001. Variational self-consistent estimates for cubic viscoplastic polycrystals: the effects of grain anisotropy and shape. J. Mech. Phys. Solids 49 (2), 313–340.
Neil, C.J., Agnew, S.R., 2009. Crystal plasticity-based forming limit prediction for non-cubic metals: application to Mg alloy AZ31B. Int. J. Plast. 25, 379–398.
Reuss, A., 1929. Berechung der Fließgrenze von Mischkristallen auf Grund der Plastizitätsbedingung für Einkristalle. Z. Angew. Math. Mech. 9, 49–58.
Rice, J.R., 1976. The localization of plastic deformation. In: 14th International Congress of Theoretical and Applied Mechanics, pp. 207–220.
Schwindt, C., Schlosser, F., Bertinetti, M.A., Signorelli, J.W., 2015. Experimental and Visco-Plastic Self-consistent evaluation of forming limit diagrams for anisotropic sheet metals: an efficient and robust implementation of the M-K model. Int. J. Plast. 73, 62–99.
Serenelli, M.J., Bertinetti, M.A., Signorelli, J.W., 2010. Investigation of the dislocation slip assumption on formability of BCC sheet metals. Int. J. Mech. Sci. 52 (12), 1723–1734.
Serenelli, M.J., Bertinetti, M.A., Signorelli, J.W., 2011. Study of limit strains for FCC and BCC sheet metal using polycrystal plasticity. Int. J. Plast. 7–8, 1109–1119.
Signorelli, J.W., Bertinetti, M.A., Turner, P.A., 2009. Predictions of forming limit diagrams using a rate-dependent polycrystal self-consistent plasticity model. Int. J. Plast. 25, 1–25.
Signorelli, J.W., Serenelli, M.J., Bertinetti, M.A., 2012. Experimental and numerical study of the role of crystallographic texture on the formability of an electro-galvanized steel sheet. J. Mat. Process. Tech. 212, 1367–1376.
Stoughton, T.B., Yoon, J.W., 2011. A new approach for failure criterion for sheet metals. Int. J. Plast. 27, 440–459.
Stoughton, T.B., Zhu, X., 2004. Review of theoretical models of the strain-based FLD and their relevance to the stress-based FLD. Int. J. Plast. 20, 1463–1486.
Tadano, Y., Yoshida, K., Kuroda, M., 2013. Plastic flow localization analysis of heterogeneous materials using homogenization-based finite element method. Int. J. Mech. Sci. 72, 63–74.
Takahashi, H., 1988. Predictions of plastic stress-strain relations of polycrystals based on the Lin model. Int. J. Plast. 4, 231–250.
Taylor, G.I., 1938. Plastic strains in metals. J. Inst. Met. 62, 307–324.
Viatkina, E.M., Brekelmans, W.A.M., Geers, M.G.D., 2005. A crystal plasticity based estimate for forming limit diagrams from textural inhomogeneities. J. Mat. Process. Tech. 168, 211–218.
Wenk, H.R., Canova, G., Molinari, A., Mecking, H., 1988. Texture development in Halite: comparison of Taylor model and self-consistent theory. Acta. Metall. 37, 2017–2029.
Wu, P.D., MacEwen, S.R., Lloyd, D.J., Neale, K.W., 2004. Effect of cube texture on sheet metal formability. Mat. Sci. Eng. A 364 (1), 182–187.
Yoshida, K., Brenner, R., Bacroix, B., Bouvier, S., 2009. Effect of regularization of Schmid law on self-consistent estimates for rate-independent plasticity of polycrystals. Eur. J. Mech. – A/Solids 28, 905–915.
Yoshida, K., Kuroda, M., 2012. Comparison of bifurcation and imperfection analyses of localized necking in rate-independent polycrystalline sheets. Int. J. Solids. Struct. 49, 2073–2084.
Zadpoor, A.A., Sinke, J., Benedictus, R., 2009. Formability prediction of high strength aluminum sheets. Int. J. Plast. 25, 2269–2297.
Zhang, L., Wang, J., 2012. Modeling the localized necking in anisotropic sheet metals. Int. J. Plast. 39, 103–118.
Zhou, Y., Neale, K.W., 1995. Predictions of forming limit diagrams using a rate-sensitive crystal plasticity model. Int. J. Mech. Sci. 37, 1–20.